

AD A 120701

VSC-TR-82-23
(SGI-R-82-058)

INVESTIGATIONS OF NEAR-SOURCE STRUCTURAL
EFFECTS ON BODY WAVES, PART I - YUCCA FLATS;
RECEIVER FUNCTIONS APPROPRIATE TO NTS;
MOTIVE FUNCTIONAL SPECIFICATIONS

GEORGE R. MELLMAN
ROBERT S. HART
GARY M. LUNDQUIST
DAVID M. HADLEY

ANNUAL TECHNICAL REPORT
SPONSORED BY

DEFENSE ADVANCED RESEARCH PROJECTS AGENCY (DOD)
ARPA ORDER No. 2551

MONITORED BY AFTAC UNDER CONTRACT F08606-79-C-0009

The views and conclusions contained in this document are those of the authors and should not be interpreted as necessarily representing the official policies, either expressed or implied, of the Defense Advanced Research Projects Agency of the United States Government.



SIERRA GEOPHYSICS

15446 BELL-RED ROAD, SUITE 400 • REDMOND, WASHINGTON 98052 • (206) 881-8833

82

10

25

088

DTIC
ELECTE
OCT 25 1982
MH

DECLASSIFICATION STATEMENT A
Approved for public release
Distribution Unlimited

DTIC FILE COPY

SIERRA GEOPHYSICS REPORT #SGI-R-82-058

AFTAC Project Authorization: VT/0710

ARPA Order No.: 2551

Contract No.: F08606-79-C-0009

Effective Date of Contract: October 1, 1978

Contract Expiration Date: March 31, 1983

Amount of Contract: \$977,653

Principal Investigators: Robert S. Hart

Gary M. Lundquist

(206) 881-8833

Program Manager: Lt. Karen L. Harrower

(202) 325-7577

VSC-TR-82-23
(SGI-R-82-058)

INVESTIGATIONS OF NEAR-SOURCE STRUCTURAL
EFFECTS ON BODY WAVES, PART I - YUCCA FLATS;
RECEIVER FUNCTIONS APPROPRIATE TO NTS;
MOTIVE FUNCTIONAL SPECIFICATIONS

GEORGE R. MELLMAN
ROBERT S. HART
GARY M. LUNDQUIST
DAVID M. HADLEY

ANNUAL TECHNICAL REPORT
SPONSORED BY

DEFENSE ADVANCED RESEARCH PROJECTS AGENCY (DOD)
ARPA ORDER No. 2551
MONITORED BY AFTAC UNDER CONTRACT F08606-79-C-0009

The views and conclusions contained in this document are those of the authors and should not be interpreted as necessarily representing the official policies, either expressed or implied, of the Defense Advanced Research Projects Agency of the United States Government.

DTIC
ELECTE
OCT 25 1982
S D H

DISTRIBUTION STATEMENT A
Approved for public release;
Distribution Unlimited

UNCLASSIFIED

SECURITY CLASSIFICATION OF THIS PAGE (When Data Entered)

REPORT DOCUMENTATION PAGE		READ INSTRUCTIONS BEFORE COMPLETING FORM
1. REPORT NUMBER VSC-TR-82-23	2. GOVT ACCESSION NO. AD-A120701	3. RECIPIENT'S CATALOG NUMBER
4. TITLE (and Subtitle) Investigations of near-source structural effects on body waves, Part I - Yucca Flats; Receiver functions appropriate to NTS; MOTIVE functional specifications		5. TYPE OF REPORT & PERIOD COVERED Annual Technical Report
7. AUTHOR(s) George R. Mellman, Robert S. Hart, Gary M. Lundquist, David M. Hadley		6. PERFORMING ORG. REPORT NUMBER SGI-R-82-058 ✓
9. PERFORMING ORGANIZATION NAME AND ADDRESS Sierra Geophysics, Inc. 15446 Bell-Red Rd. Redmond, WA 98052		8. CONTRACT OR GRANT NUMBER(s) F08606-79-C-0009
11. CONTROLLING OFFICE NAME AND ADDRESS AFTAC/VSC Patrick AFB, FL 32925		10. PROGRAM ELEMENT, PROJECT, TASK AREA & WORK UNIT NUMBERS AFTAC Project Authorization VT/0710, ARPA Order #2551
14. MONITORING AGENCY NAME & ADDRESS (if different from Controlling Office) VELA Seismological Center 312 Montgomery St. Alexandria, VA 22314		12. REPORT DATE 1982
		13. NUMBER OF PAGES 59
		15. SECURITY CLASS. (of this report) UNCLASSIFIED
		15a. DECLASSIFICATION/DOWNGRADING SCHEDULE
16. DISTRIBUTION STATEMENT (of this Report) Distribution Unlimited		
17. DISTRIBUTION STATEMENT (of the abstract entered in Block 20, if different from Report)		
18. SUPPLEMENTARY NOTES		
19. KEY WORDS (Continue on reverse side if necessary and identify by block number) Near-source structural effects Body waves Magnitude residuals		
20. ABSTRACT (Continue on reverse side if necessary and identify by block number) This annual technical report includes a detailed report on near-source structural effects on the propagation of body waves at Yucca Flats, NTS. This study was an attempt to utilize Kirchhoff integral techniques to model the structural interactions at Yucca Flats and to thus examine the question of whether the observed magnitude residuals can be completely explained by interactions with structure. The analysis determined that the general trend and the maximum amplitudes of the observed magnitude residuals can indeed be produced		

UNCLASSIFIED

SECURITY CLASSIFICATION OF THIS PAGE(When Data Entered)

by the assumed structure. Variances with the observed magnitude residual patterns do exist in the detailed aspects, however. These variances may result from either inadequacies of the structural model or limitations of the Kirchhoff approximation. Insufficient information is currently on hand to distinguish between those possibilities.

In addition, this report contains summaries of NTS receiver function determinations and progress on development of the MOTIVE moment tensor analysis package. Details on both of those studies are contained in separate, previously submitted VSC technical reports.

Accession For	
NTIS GRA&I	<input checked="checked" type="checkbox"/>
DTIC TAB	<input type="checkbox"/>
Unannounced	<input type="checkbox"/>
Justification	
By _____	
Distribution/	
Availability Codes	
Dist	Avail and/or Special
A	

UNCLASSIFIED

SECURITY CLASSIFICATION OF THIS PAGE(When Data Entered)

TABLE OF CONTENTS

	<u>Page</u>
I. EXECUTIVE SUMMARY.	1
II. INVESTIGATIONS OF NEAR SOURCE EFFECTS ON BODY WAVES, PART 1 - YUCCA FLATS.	3
III. RECEIVER FUNCTIONS APPROPRIATE TO NTS.	53
IV. MOTIVE FUNCTIONAL SPECIFICATIONS	56
V. REFERENCES	59

LIST OF FIGURES AND TABLES

<u>FIGURE/TABLE</u>	<u>Page</u>
Figure 1. (after Alewine et al., 1977) Residuals of observed vs. predicted M_b for sources within Yucca Valley	4
Figure 2. Contour map of Cenozoic-Paleozoic contact for Yucca Flats as determined by Herrin et al. Line A-A' corresponds to cross section shown in modeling plots. Locations 1-9 are selected events used in waveform comparisons.	14
Figure 3. (after Herrin et al.) Profile used for two dimensional model of southern portion of basin. Above are shown M_b residuals for sources south of $37^{\circ}5'$	15
Table 1. Material Properties for Yucca Flats Model	17
Figure 4. Expanded version of Figure 2 showing contour map of the Cenozoic-Paleozoic contact. Numbers on line A-A' indicate source locations for synthetic seismograms.	18
Figure 5. Cross section A-A' and grid for northern basin model, showing surface, Cenozoic-Paleozoic boundary and source locations. Arrow indicates direction of propagation of plane wave in reciprocal problem	19
Figure 6. Step function response for teleseismic receiver ($p = .07$ sec/km) west of basin. Number of response corresponds to source location number in Figure 5	22
Figure 7. Far field seismograms for model in Figure 5 and Ricker wavelet source with time constant of 1 sec	23
Figure 8. Synthetic seismograms for model in Figure 5 using SRO instrument, von Seggern-Blandford source function with $k = 10$, $B = 2$ receiver function for station E from E. Kazakh events and additional attenuation operator with $t^* = .6$ sec. Western azimuth	24
Figure 9. As in Figure 5, but for North azimuth	25
Figure 10. Step function responses for North azimuth.	26

<u>FIGURE/TABLE</u>	<u>Page</u>
Figure 11. Ricker wavelet synthetic seismograms for North azimuth	27
Figure 12. Synthetic seismograms, as in Figure 8 but for North azimuth.	28
Figure 13. Model as in Figure 5, but for East azimuth . . .	29
Figure 14. Step function responses for East azimuth	30
Figure 15. Ricker wavelet synthetic seismograms for East azimuth	31
Figure 16. Synthetic seismograms, as in Figure 8 but for East azimuth	32
Table 2. NTS Predicted Magnitude Anomalies	34
Figure 17. (after Alewine et al., 1977) Observed magnitude residuals for Yucca Flats.	36
Figure 18. Expanded version of Figure 2 showing depth to Cenozoic-Paleozoic contact, in km. Line A-A' corresponds to cross sections in Figures 5, 9, and 13, with source locations of events used for waveform comparisons	37
Figure 19. Waveforms of events proceeding east to west across basin, recorded at station ZOBO. Note development of interference effect on back of second peak. Traces scaled to equal amplitude by plotting routine.	39
Figure 20. Waveforms recorded at station MAJO for events proceeding west to east across the basin	40
Figure 21. Waveforms recorded at station NAO for events proceeding west to east across basin.	41
Figure 22. Herrin et al. profile E-3, used as cross section for two-dimensional southern basin model. Grid shown for surface, water table and Paleozoic interface. Sources located directly below water table. For receiver at northern or southern azimuth.	43
Figure 23. Step function responses for model in Figure 23 at north or south azimuth	44

<u>FIGURE/TABLE</u>	<u>Page</u>
Figure 24. Ricker wavelet source synthetics for model in Figure 22 and receiver at north or south azimuth	45
Figure 25. Synthetic seismograms for explosion sources, as in Figure 8, but for model in Figure 22 with receiver at north or south azimuth.	46
Figure 26. Model as in Figure 22 but for receiver at east azimuth.	47
Figure 27. Step function responses for sources in Figure 26. Receiver at east azimuth	48
Figure 28. Ricker wavelet synthetic seismograms for model in Figure 26. Receiver is at east azimuth with $p = .07$ sec/km	49
Figure 29. Synthetic seismograms as in Figure 8 but with model in Figure 26. Receiver is at east azimuth	50

I. EXECUTIVE SUMMARY

The VSC research program at Sierra Geophysics during FY81 was sub-divided into three distinct tasks. These tasks, summarized below, have the common link of extending our understanding of body wave propagation from underground explosions and thus enhancing the utility of those seismic phases in the yield estimation procedure.

The first task of this past year's program was the determination of receiver functions at a number of seismic stations for back-azimuths appropriate to the Nevada Test Site. While most of the seismic stations of interest are not well situated for the purpose of monitoring NTS, an attempt to extend the receiver function methodology to NTS azimuths represents an important test of the analysis technique. This research task was presented in detail in the Sierra Geophysics Semi-Annual Technical Report for the period December 1, 1980 to May 31, 1981 submitted to AFTAC/VSC [VSC-TR-81-26 (SGI-R-81-041)]. A summary of that research is contained in Section III of this report.

The second task of the FY81 program was an attempt to model the effects of near-source structural effects on body waves from underground explosions. These effects at NTS had been examined previously and modeling attempted (Hart et al., 1979) using preliminary structural information and an optics approach to propagation. In this program, more reliable structural models were available as well as a more sophisticated Kirchhoff integral equation method. Two source regions of interest were examined. The results of modeling propagation in the first area, Yucca Flats at NTS, are presented in detail in Section II of this report. Also presented is a summary of the theoretical background of the Kirchhoff integral method. The results of the application of this

technique to a second test area are presented in Part II of this report, submitted separately.

Finally, the third phase of the FY81 research program was the initiation of a long term project to develop a moment tensor analysis package (called MOTIVE) to jointly invert surface waves and body waves. This package will be able to incorporate the most advanced path corrections for both data types and is intended for use in both seismic discrimination and yield estimation procedures. This task will also determine preliminary moment vs. yield relationships. This phase began toward the end of the third quarter of FY81 and is still basically in its preliminary stages. A summary of the approach to the software development is contained in Section IV of this report. A detailed presentation of the functional specifications of the package may be found in a separate technical report submitted to AFTAC/VSC [VSC-TR-81-022 (SGI-R-81-039)].

II. INVESTIGATIONS OF NEAR SOURCE EFFECTS ON BODY WAVES, PART I - YUCCA FLATS

1. Introduction

It has been appreciated for some time that observed teleseismic magnitudes of underground nuclear explosions at Yucca Flats differ systematically from magnitudes predicted on the basis of known yields (Alewine et al., 1977). Figure 1 shows a contour map of the observed magnitude residuals. In general, contours trend north-south, parallel to the strike of the Yucca basin, with anomalously large observed m_b occurring for events in the western portion of the basin. This strongly suggests that the observed magnitude anomalies are associated with shallow basin structure.

There are two simple mechanisms which might be invoked to explain these observed anomalies. The first mechanism is simply a systematic east-west change in material properties at the working points of the underground explosions in question. This would result in changes of coupling, and therefore changes in apparent yield as locations change in the basin. One might expect, however, that this systematic variation would have been detected in the borehole logs. The second mechanism is a focusing and defocusing of reflections and transmissions by interfaces which vary in depth throughout the basin. In this study, we will restrict ourselves to this second mechanism, and examine the effects of known basin structures on both waveform and amplitude for a number of source sites throughout the Yucca Flats basin.

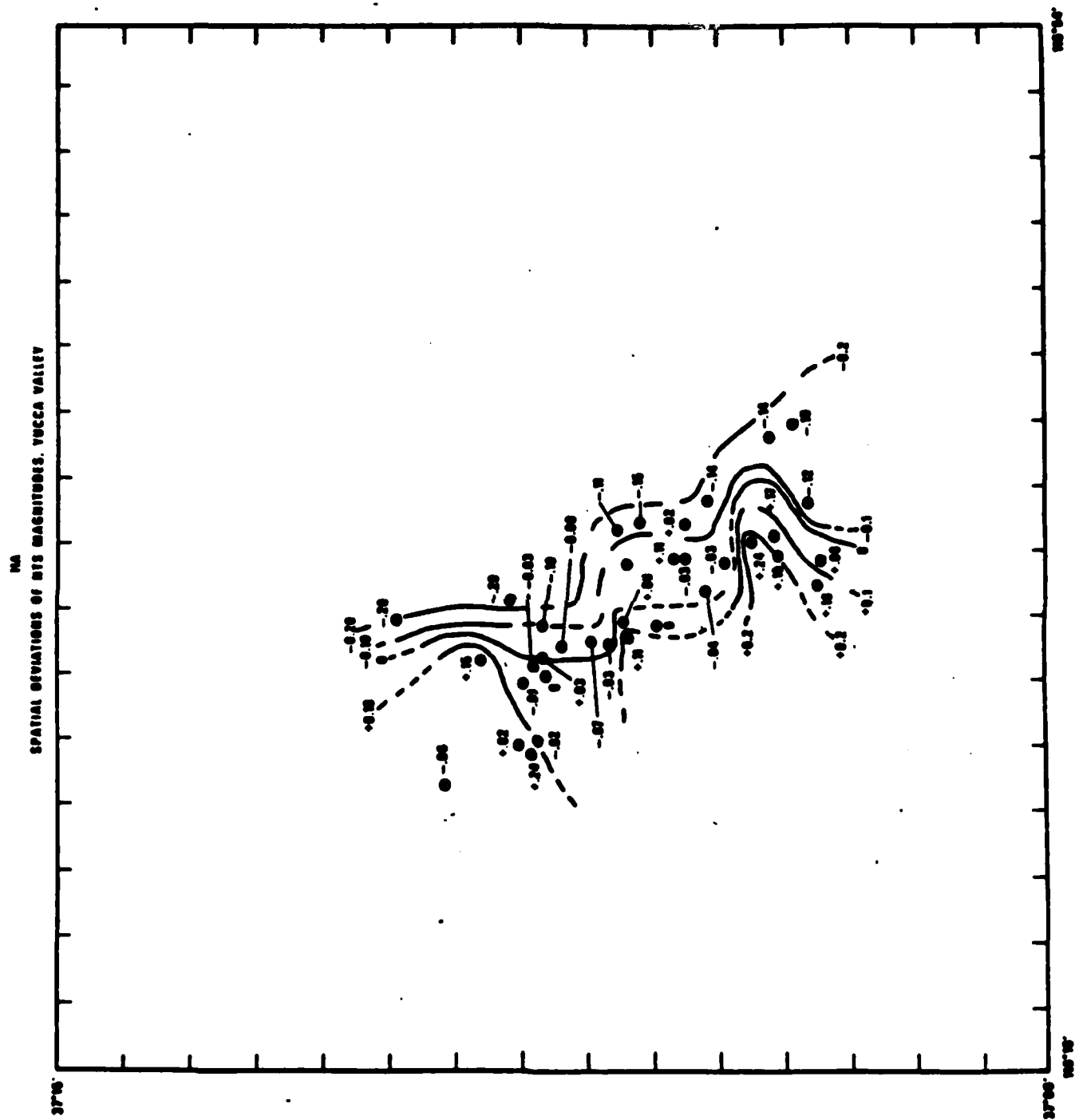


Figure 1. (after Alewine, et al., 1977) Residuals of observed vs. predicted M_b for sources within Yucca Valley.

In the next section of this report we describe the Kirchhoff approximation, the specific Boundary Integral Equation method used in this work to solve the wave propagation problem. The emphasis of this work is on applications of this method. A thorough mathematical treatment of several Boundary Integral Equation methods, including the Kirchhoff approximation, is given elsewhere (Wyss and Mellman, 1982), and thus an heuristic, rather than mathematical, approach is used in this discussion. The aim of this section is to provide the reader with a simple description of the methods used in this work and the applicability of these methods, rather than providing a detailed mathematical treatment.

In the third section we examine the synthetic seismograms produced using the Kirchhoff approximation on existing Yucca Basin models, and compare these synthetic seismograms to observed data. No attempt has been made to model details of specific events, as this would have involved detailed source modeling far beyond the scope of the current project. In addition, uncertainties in available basin structures and uncertainties in the effects of near-source non-linearities make the results of such detailed studies uncertain, at best. Instead, we examine only the broad trends exhibited by the data. These trends take the form of a systematic east to west magnitude bias and an east to west evolution of wave shape. A comparison of synthetic seismograms with data indicate that known structure is sufficient to explain both magnitude and waveform changes in the broad sense.

2. The Kirchhoff Approximation

The efficient numerical propagation of waves through irregular layers of constant material in two and three dimensions has been a problem of considerable geophysical interest of the last few years, and has received a great deal of theoretical consideration. However, even for the case of acoustic wave propagation, this problem has been particularly difficult numerically. This is primarily due to the fact that although the equations of motion are linear in the field quantities of displacement and velocity, they are non-linear in terms of interface structure. This fundamental non-linearity precludes the construction of solutions for complex structures by superposition of the solutions for simple structures, and forces one into computationally costly schemes.

Techniques for dealing with this difficulty have run the gamut from classical ray techniques to finite difference codes, with no single technique proving entirely satisfactory. In cases where significant diffraction and interference effects are present, an "exact" solution is required and finite difference methods have generally been employed. Unfortunately, these computational techniques are well known for their heavy computational demands even in two dimensions, and their seemingly inevitable use in certain problems has forced the numerical community into requiring ever larger and faster computers.

The large computational requirements of finite difference methods are created by the necessity of imposing a grid on a large volume of space. For problems involving wave propagation in irregular layers of constant velocity material, however, a more concise and efficient formulation is possible. This formulation leads to Boundary Integral Equation (BIE) techniques, which require the gridding of surfaces of

velocity discontinuity only. This results in a much smaller number of total grid points in BIE calculations, as opposed to the corresponding finite difference calculations. The penalty that must be paid for this reduction in the number of grid points is that the matrices which describe the equations of motion and boundary conditions, while sparse in finite difference calculations, are dense for BIE methods. These dense matrices are a significant problem in the implementation of BIE methods, and force one into a careful consideration of how to deal with them.

A useful approximation at this point is the separation of the BIE problem into two parts. The first part is the propagation of the wave field from one discontinuity to an adjacent discontinuity. The second part consists of the interaction of the wave field with the discontinuity.

The first, or propagation, stage may be considered simply in terms of the propagation problem of a point source in a whole space. Each grid point on the first boundary represents a point source in the whole space, and each grid point on the second, or receiving, boundary acts as a receiver in a whole space. Thus, the response that the receiver boundary, ignoring boundary interaction, may be given exactly by

$$u(\mathbf{x}) = \int_{\substack{\mathbf{x}_o \in S_1}} \left(u(\mathbf{x}_o) \frac{\partial G}{\partial n}(\mathbf{x}, \mathbf{x}_o) - \frac{\partial u}{\partial n}(\mathbf{x}_o) G(\mathbf{x}, \mathbf{x}_o) \right) dS_1 \quad (1)$$

where G is the whole space Green's functions and n is the unit normal to the surface S_1 at \mathbf{x}_o . If the separation between source and receiver surfaces is never less than approximately one grid point spacing, a

stable and accurate time domain estimate of $u(x)$ and $\partial u(x)/\partial n$ may be obtained in a simple straightforward manner.

The second, or interaction stage, may be approached in several ways. In this study, we use the simplest treatment of the interaction, which is known as the Kirchhoff approximation. In this approximation, only the local values of the wave field and the local direction of the surface normal are considered. Thus, at each point, the interaction of the incident wave with the surface is calculated as if the local portion of the incident wave were part of a plane wave and the local boundary were in fact a plane boundary with normal direction equal to the local boundary normal. The direction and amplitude of the equivalent incident plane wave at each said point at a single point in time must be calculated from the values of $\partial u/\partial n$ and $\partial u/\partial t$ of the incident wave field at the appropriate space and time point. Boundary values of the field variables may then be computed through simple local use of plane wave reflection and transmission coefficients. In general, these coefficients will change as a function of both time and position on the surface.

It is a relatively simple matter to cascade the two boundary procedure and in this way obtain propagation through a stack of layers. Thus, if we number our interfaces 1 through N, with an input wave incident on layer 1, we apply the two boundary procedure first to interfaces 1 and 2, and then use the newly computed boundary values at interface 2 to propagate the wavefield to layer 3. This procedure is continued until interface N is reached. In each case, the Green's function used is the whole space Green's function appropriate for the material through which propagation is currently taking place.

First order reflection may be included in the solution in a relatively simple manner. Beginning at interface N, we propagate the boundary values previously calculated at interface N to interface N-1. The sum of these boundary values and the boundary values computed as a result of propagation from interface N-2 now form the new estimate of the boundary values at interface N-1. This new estimate is then used to propagate the reflected wavefield to layer N-2. This procedure is repeated until interface 1 is encountered. At interface M, we have estimates of the boundary values resulting from propagation from interface M-1 and estimates of the boundary values resulting from propagation from interface M+1. The total boundary values at interface M are a sum of these quantities. By repeating the propagation procedure "up" and "down" the stack of layers and updating the appropriate "upgoing" and "downgoing" boundary values at each interface, it is possible to include multiple reflections to any desired order. This procedure may be viewed as a kind of ray expansion for BIE methods. It has the advantage that no more than two interfaces need be considered at a time, and that the amount of computation required is linearly proportional to both the order number of the multiple reflections desired and the number of layers in the stack.

The Kirchhoff approximation bears a strong resemblance, in many ways, to geometric optics. In fact, it is possible to derive geometric optics as a high frequency approximation to the Kirchhoff BIE formulation. Thus, the Kirchhoff approximation may be expected to be very accurate, subject to restrictions imposed by the finite grid, in domains where optics is valid. Unlike optics, the Kirchhoff approximation does not show abrupt, discontinuous behavior at shadow zone boundaries,

instead showing the continuous, frequency dependent behavior one expects from diffraction theory.

In general, the Kirchhoff approximation gives very accurate results in situations dominated by kinematic effects. Where dynamic effects are important, the results become increasingly inaccurate. By dynamic effects, we mean those effects caused by multiple interactions of the wavefield with a boundary. Examples of such effects include head waves and diffraction of post-critical waves. It is somewhat difficult to assess exactly where the Kirchhoff approximation becomes inaccurate, since arrivals usually have the correct arrival time, although possibly an incorrect amplitude. Thus, the Kirchhoff approximation usually gives plausible, if not necessarily correct, results. The question of accuracy of various BIE techniques is considered further in Wyss and Mellman (1982).

Two models of the Yucca Basin have been considered in this work. The northern model is smooth and does not have radically dipping structures. It is felt that the Kirchhoff approximation provides very accurate results for this case. The southern model contains faults and a steeply dipping sidewall. Reflected energy for sources near the sidewall is well beyond critical angle. For this reason, the results of the southern model calculations should be treated as somewhat suspect. Additional work with more accurate BIE methods is necessary for this southern model in order to assess the reliability of our results.

Several additional approximations and transformations proved desirable in the current study. Since the problem of interest involves numerous sources observed at relatively few teleseismic receivers, a reciprocal calculation is much more efficient than the solution of the

true problem. If $G_{ij}(x, x')$ is the displacement in the i direction at point x caused by a point force in the j direction at point x' then, by reciprocity (Aki and Richards, 1979)

$$G_{ij}(x, x') = G_{ji}(x', x) \quad (2)$$

Differentiating we find

$$G_{ij,j}(x, x') = G_{ji,j}(x', x). \quad (3)$$

Thus, the equivalent problem to determining the vertical displacement at x caused by an explosion at x' is to find the divergence of the displacement at x' caused by a vertical point force at x . Letting the displacement at x' be \underline{u} , we have, in terms to the usual potential decomposition

$$\underline{u} = \nabla \phi + \nabla x \underline{A}, \text{ or}$$

$$\nabla \cdot \underline{u} = \nabla^2 \phi = \frac{1}{c^2} \frac{\partial^2 \phi}{\partial t^2}. \quad (4)$$

Thus we may find the vertical displacement at a distant receiver for an explosion source in a basin by taking the second time derivative of the dilatational potential at the source point induced by a vertical point force at the receiver point. For receivers in the 30°-90° distance range, this reciprocal problem amounts to determining the dilatational potential at all possible source points for a plane wave incident on the basin structure. This is not the same as simply interchanging the source and receiver points.

As only the dilatational potential contributes to the final result, and since we will consider only a short time window following the P-wave first arrival, the only shear wave energy that contributes to the final solution must undergo at least two mode conversions. As this is not an efficient process, and as such energy will in any case be somewhat late in the record, we do not include shear conversions. Correct elastic reflection coefficients are used, however, so that energy lost from P-waves due to such conversions is accounted for.

Since we are modeling only a restricted portion of the seismogram, no attempt has been made to suppress arrivals due to grid edge effects. Such arrivals are quite evident and generally occur several seconds after the first arrival.

All synthetic seismograms presented in this study include up to second order reflections, which includes all "rays" undergoing a total of five or fewer reflections. This proved sufficient in terms of the time window of interest and constraints imposed by the arrival of the edge "reflection".

3. Yucca Flats

The basin structure is dominated by two discontinuities. The shallower of these, corresponding to the location of the water table, is known via well logs to occur at a more or less constant depth of about 500 m. throughout the basin. The deeper discontinuity, which represents the Cenozoic-Paleozoic basement contact, has been extensively studied by Herrin and Goforth (1981), using a combination of data from three seismic lines and gravity data acquired throughout the basin. A joint inversion was performed by Herrin and his colleagues which, in effect, used the gravity data to interpolate between the seismic data. A contour map of the resulting model may be seen in Figure 2.

The northern portion of the Herrin model in Figure 2 is suitable for use, with minor modification, in our basin model. This is not true of the southern portion, since the abrupt eastern sidewall is apparently caused by a lack of data, rather than representing an actual feature of the basin. As the steepness of the basin sidewalls has a major effect on both amplitudes and waveforms for sources throughout the basin, it was decided to use a two-dimensional model based on Herrin's profile E-3, shown in Figure 3, to represent the southern portion of the basin, rather than the inversion result. An examination of Figure 2 shows that the two dimensional approximation used for the southern portion of the basin is well justified by the three-dimensional model.

We will first consider sources in the northern portion of the basin. The model used is essentially the Herrin and Goforth model of the Paleozoic-Cenozoic contact with slight changes necessitated by the numerical requirements of the Kirchhoff integral code. Numerical instabilities due to inadequate surface sampling can result if the distance

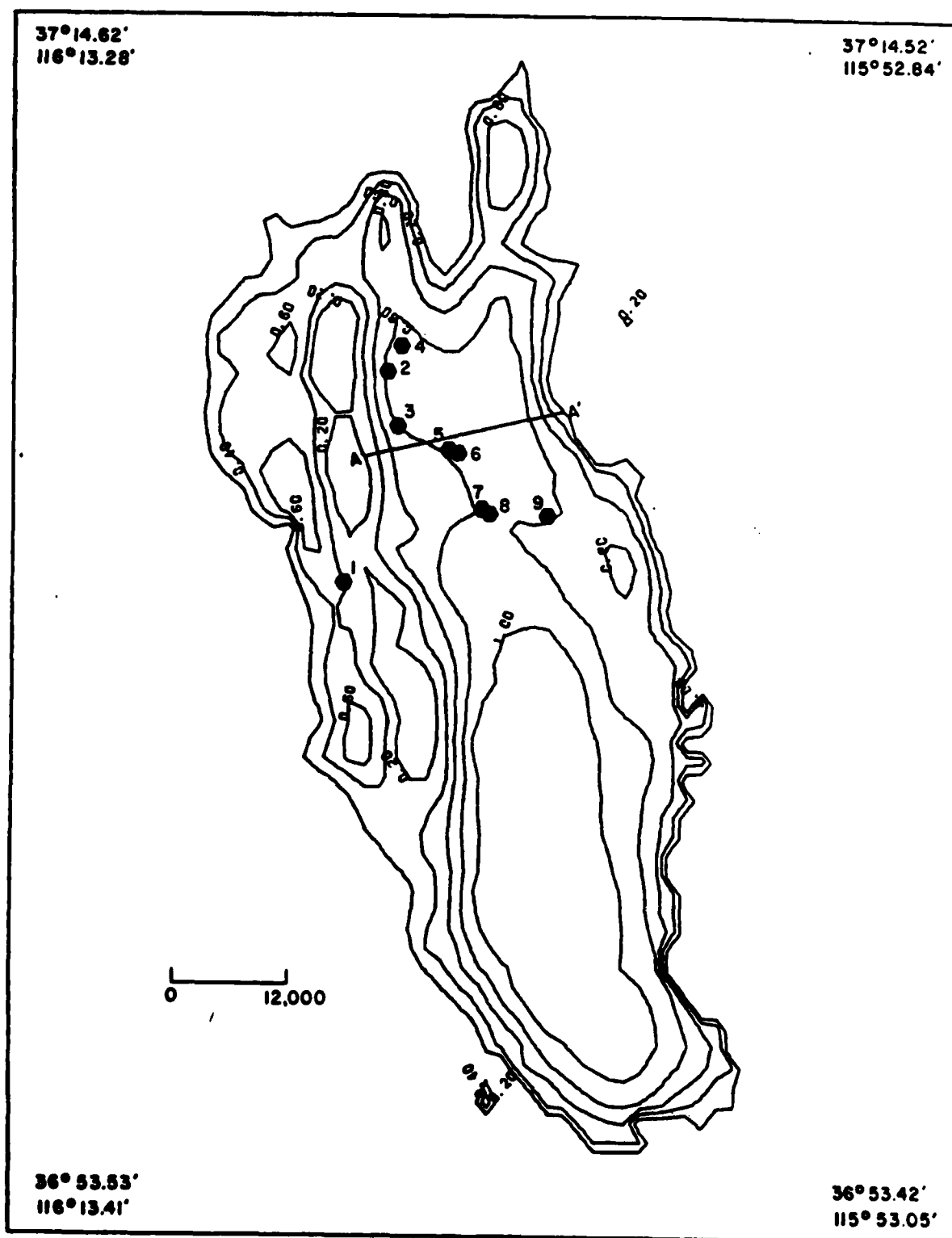


Figure 2. Contour map of Cenozoic-Paleozoic contact for Yucca Flats as determined by Herrin et al. Line A-A' corresponds to cross section shown in modeling plots. Locations 1-9 are selected events used in waveform comparisons.

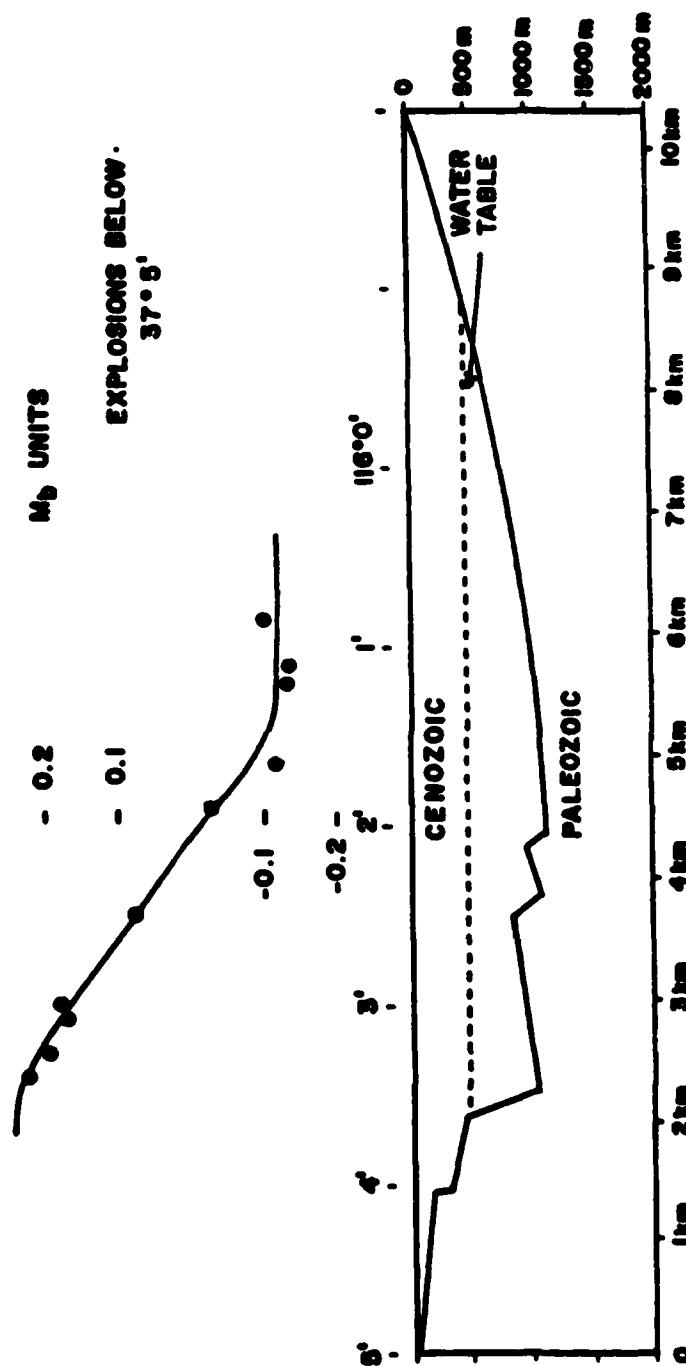


Figure 3. (after Herrin et al.) Profile used for two dimensional model of southern portion of basin. Above are shown M_b residuals for sources south of $37^{\circ} 5'$.

between boundaries becomes appreciably less than the surface sampling distance. For this reason, the sides of the basin were tapered at a depth of 200 m., rather than allowing the tuff layer to pinch out, as occurs in the Herrin model. Also, in order to minimize the effects of the boundary modification, it was necessary to exclude the water table interface from the model and use an average of saturated and unsaturated material properties, shown in Table 1, for the tuff layer. The alternative would have been to taper the basin at 400 m., which would have had a more noticeable effect on the results than the course chosen.

Source locations were chosen on a line A-A', shown on Figure 4, and were uniformly placed at a depth of 550 m. The line A-A' was chosen to be perpendicular to the major axis of the basin, in a region which is essentially two-dimensional in nature. This allows for results obtained on line A-A' to be applied to nearby source locations with some degree of confidence. A cross-section view, along line A-A', of the model is shown in Figure 5. Squares represent grid points, while the normals to the surface at each grid point designated by a short line segment at each grid point. Source locations are shown as an intermediate layer, and are numbered from east to west. We note that even grid point spacing is not a requirement of the program, and that irregular spacing has been employed to provide improved accuracy and efficiency.

Since seismograms are to be computed for a number of source locations but only relatively few receiver locations, computational effort

TABLE 1

Material Properties for Yucca Flats Models

Northern Model

Layer No.	V_p	V_s	ϵ
1	2.4	1.4	2.2
2	4.8	2.8	2.6

Southern Model

Layer No.	V_p	V_s	ϵ
1	2.1	1.2	1.8
2	3.0	1.8	2.2
3	4.8	2.8	2.6

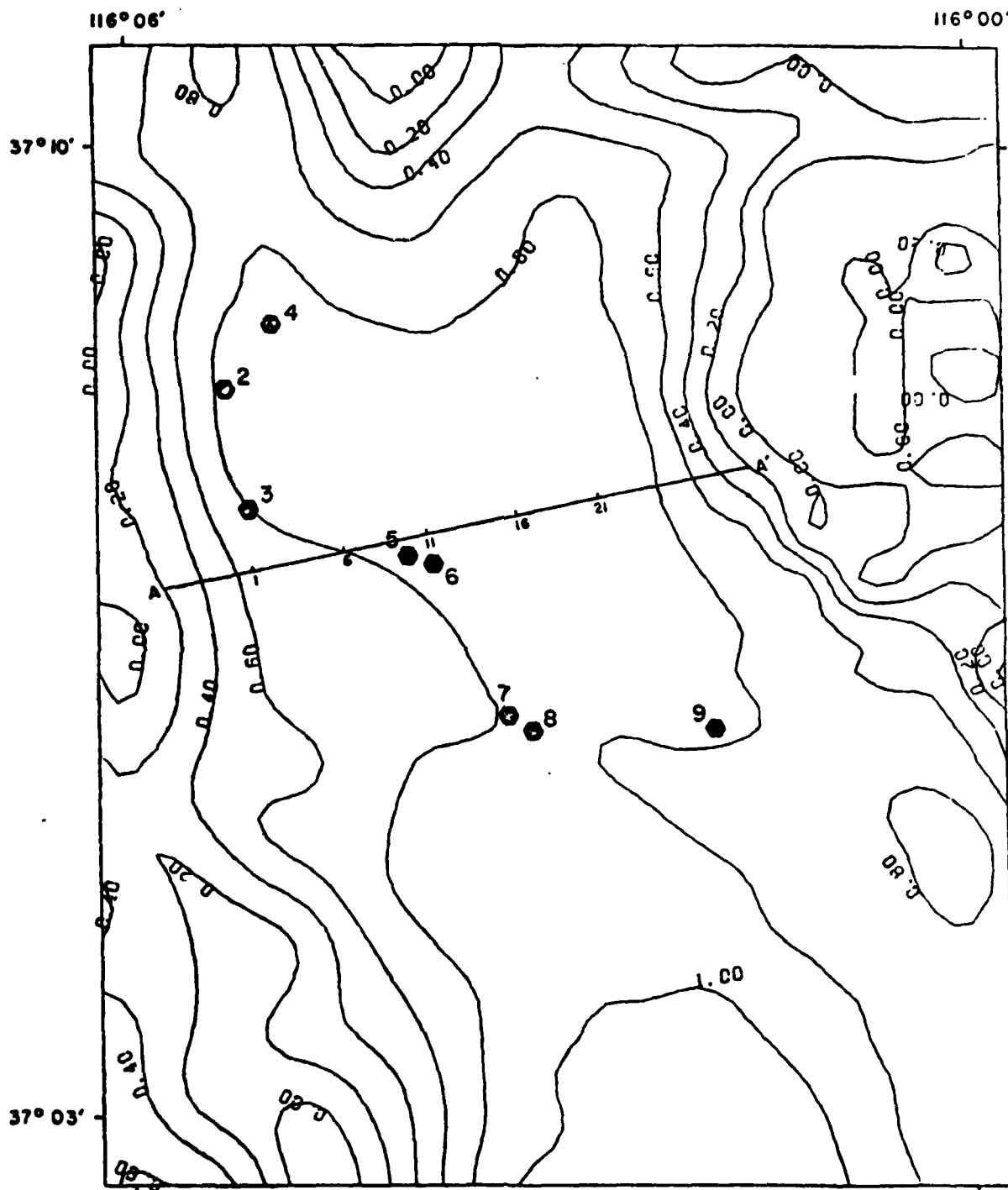


Figure 4. Expanded version of Figure 2 showing contour map of the Cenozoic-Paleozoic contact. Numbers on line A-A' indicate source locations for synthetic seismograms.

NTS BASIN WEST AZIMUTH

MAX SPACE=0.3330

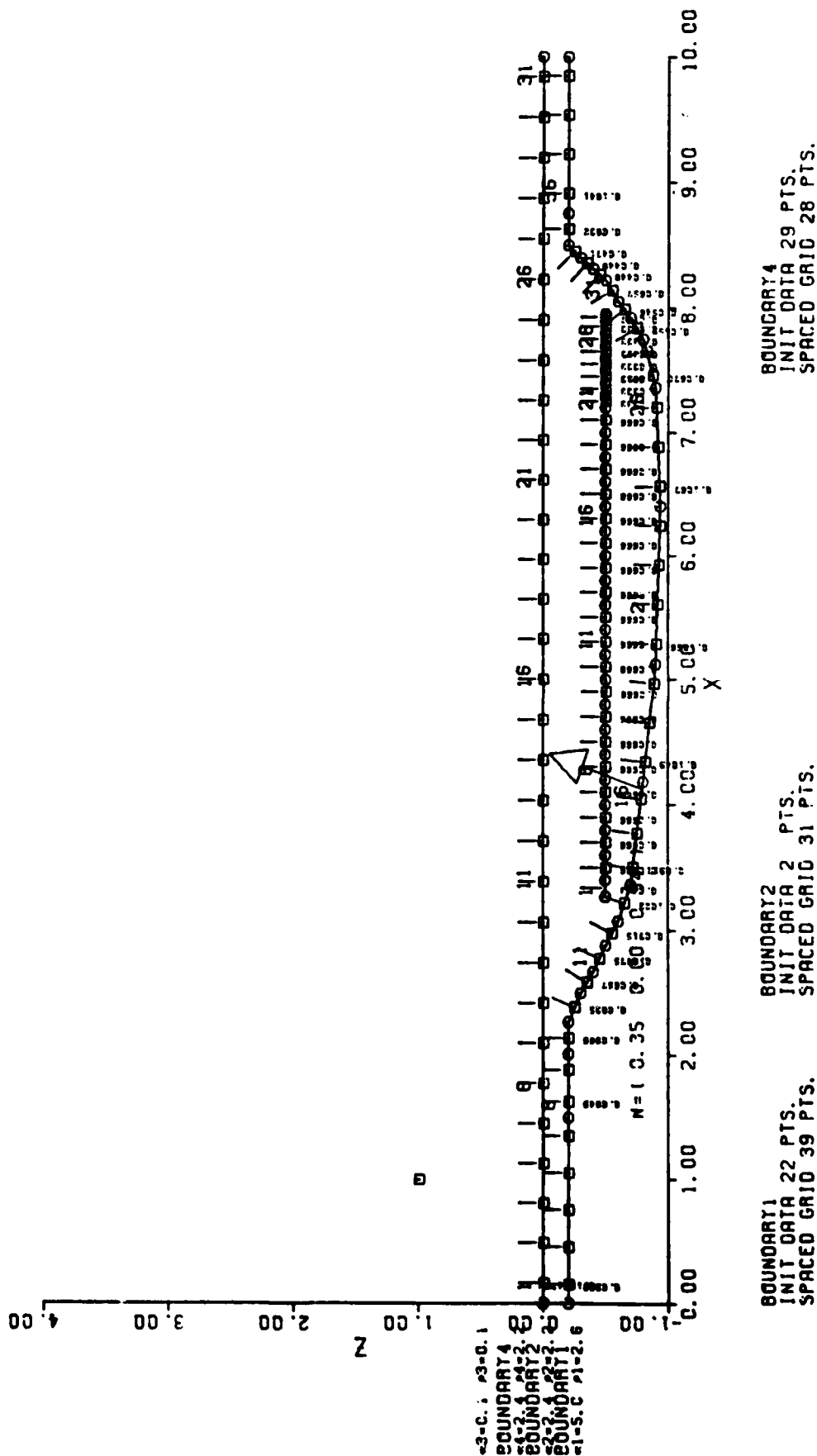


Figure 5. Cross section A-A' and grid for northern basin model, showing surface, Cenozoic-Paleozoic boundary and source locations. Arrow indicates direction of propagation of plane wave in reciprocal problem.

can be greatly reduced by employing a reciprocal calculation scheme. Incident plane waves, with ray parameter $p = .07$ sec/km, corresponding to a distance of about 60 degrees were used for the incoming energy. Three azimuths were utilized, and have for simplicity been labeled west, north, and east, although the true directions are parallel and perpendicular to the line A-A' and thus are oriented about 20 degrees from the nominal compass directions. In all cases, reflections up to order two, which may include as many as five reflections, have been included.

For each azimuth, we present a set of four figures. The first of these shows the model, with an arrow indicating the direction of propagation of the reciprocal plane wave. The second figure shows the step function response at the far field station for every fifth source location on line A-A'. The third figure is a synthetic seismogram produced by convolving the time derivative of the step function response shown in the second figure with a Ricker wavelet with time constant of one second. The Ricker wavelet has the form $d/dt(e^{-\alpha t^2})$, and provides a simple means of producing realistic synthetic seismograms. The fourth figure in each set contains true synthetic seismograms, consisting of the time derivative of the step function responses (shown in the second figure) convolved with a von Seggern and Blandford (1972) time function with $k = 10$ and $B = 2$, an attenuation operator (Futterman, 1966) characterized by $t^* = .6$, a typical relatively simple receiver function and a KS 36000 instrument response.

The western azimuth is shown in Figures 5 through 8. As expected, the step responses in Figure 6 show delays in arrival time as the source moves to the east. The arrival from source location 1 appears somewhat larger than the arrival from source 6, probably due to focusing of the direct ray by the western portion basin. There is also a small change in pP time between sources 1 and 6, which is denoted by a return to zero of the step response due, as before, to the western sidewall. The most significant feature, however, is the change in arrival time and amplitude of the second negative phase, which represents a large reflection off the bottom and side of the basin. Due to focusing, this arrival is very large and early for source 1, becoming progressively smaller and more delayed for sources toward the center of the basin (e.g., source 16). This arrival then increases in amplitude and its delay lessens for sources near the eastern side of the basin, a result of focusing of the reflection off the eastern wall.

A second order positive reflection may also be seen, particularly for source 16, although this phase arrives too late to have an effect on the early portion of the waveform (and, hence, on m_b). The final arrival, a ramp function, is a truncation phase caused by "reflections" off the edge of the model. Fortunately, this phase arrives with sufficiently large time delay and with sufficiently long period that it does not significantly affect the synthetic seismograms.

The influences of the multiple reflections are quite obvious in Figures 7 and 8. The large, early reflection for source 1 interferes constructively and produces a very large, narrow first trough and second peak in the waveform. The greater delay for source 6 results in broadening of the waveform in general and an attendant decrease in

NTS BASIN
WEST AZIMUTH

ROW COL

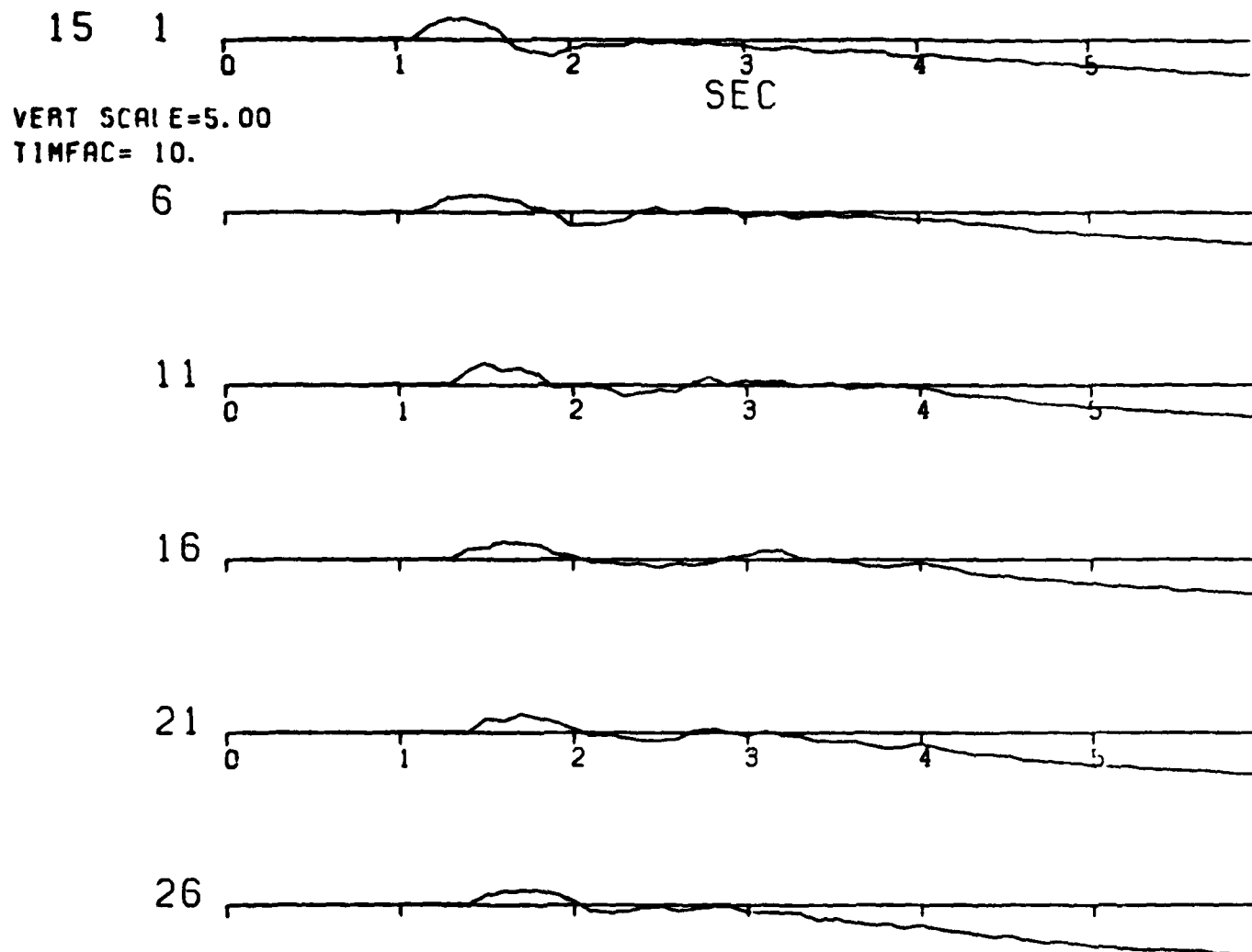


Figure 6. Step function response for teleseismic receiver ($p = .07$ sec/km) west of basin. Number of response corresponds to source location number in Figure 5.

NTS BASIN-WEST AZIMUTH
WAVELET SOURCE

23

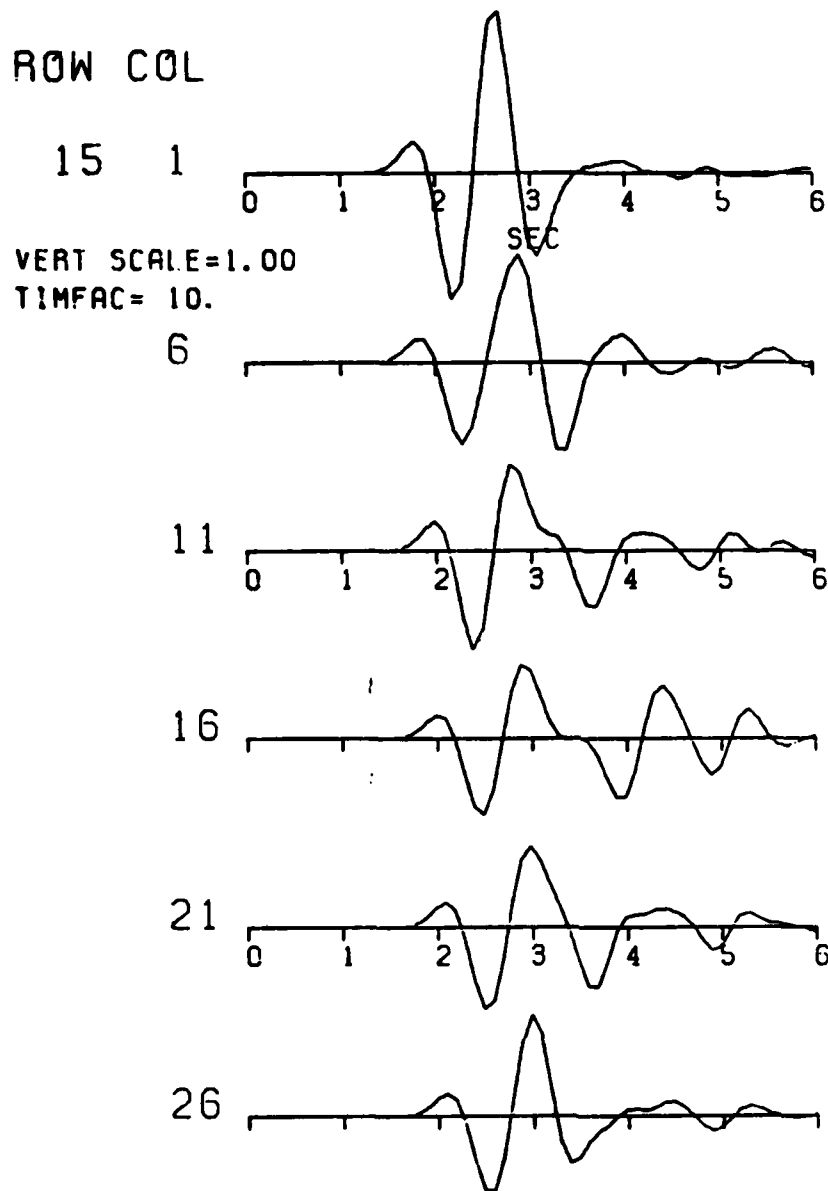


Figure 7. Far field seismograms for model in Figure 5 and Ricker wavelet source with time constant of 1 sec.

NTS BASIN-WEST AZIMUTH EXPLOSION SOURCE

24

ROW COL

15 1

VERT SCALE=1.00
TIMFAC= 10.

6

11

16

21

26

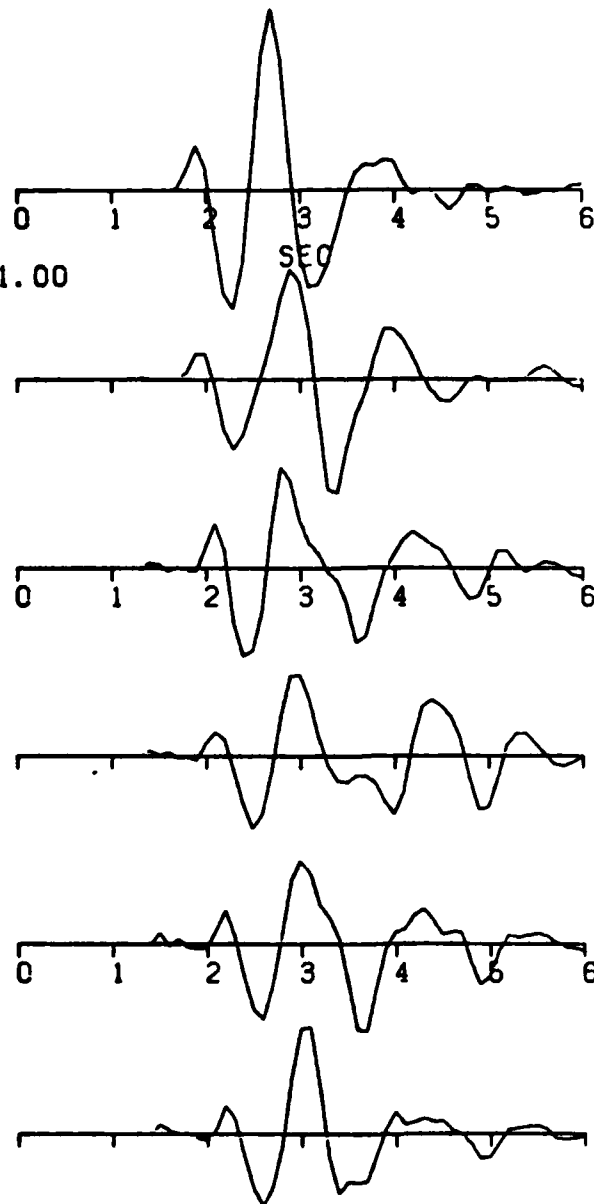


Figure 8. Synthetic seismograms for model in Figure 5 using SRO instrument, von Seggern-Blandford source function with $k = 10$, $B = 2$, receiver function for station E from E. Kazakh events and additional attenuation operator with $t^* = .6$ sec. Western azimuth.

NTS BASIN NORTH AZIMUTH

MAX SPACE=0.3330

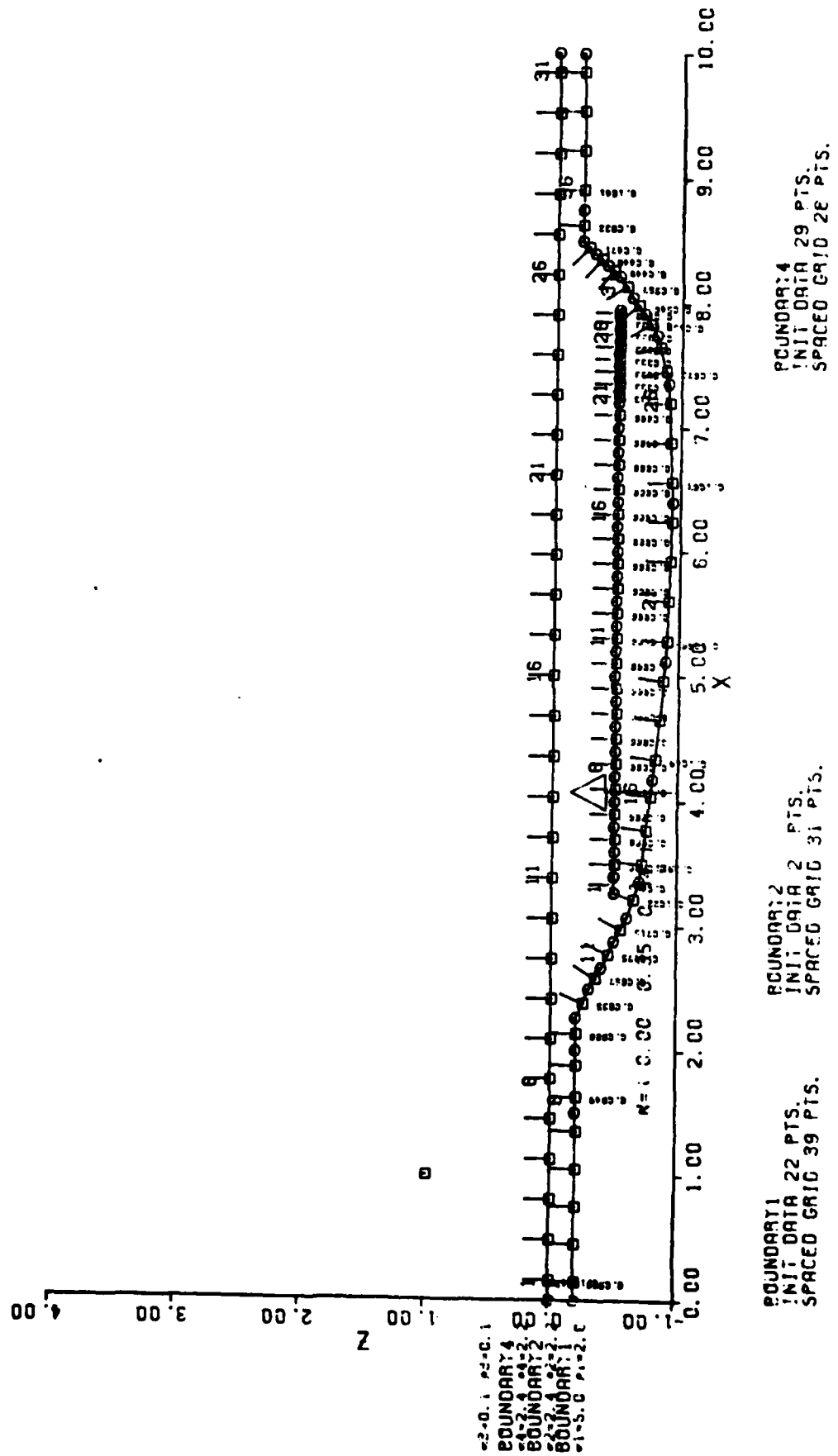
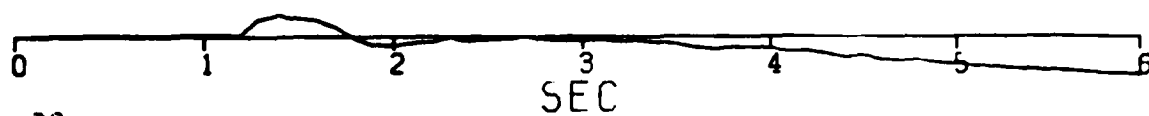


Figure 9. As in Figure 5, but for North azimuth.

NTS BASIN
NORTH AZIMUTH

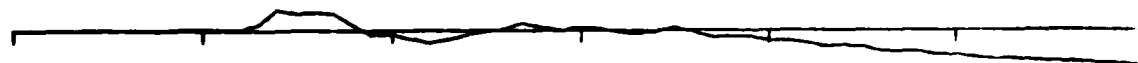
ROW COL

15 1

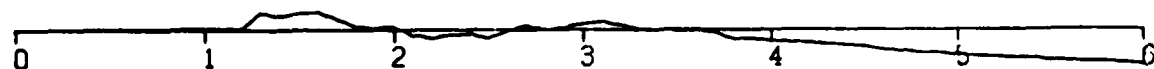


VERT SCALE=5.00
TIME=10.

6



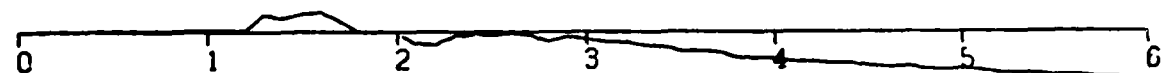
11



16



21



26



Figure 10. Step function responses for North azimuth.

NTS BASIN-NORTH AZIMUTH
WAVELET SOURCE

ROW COL

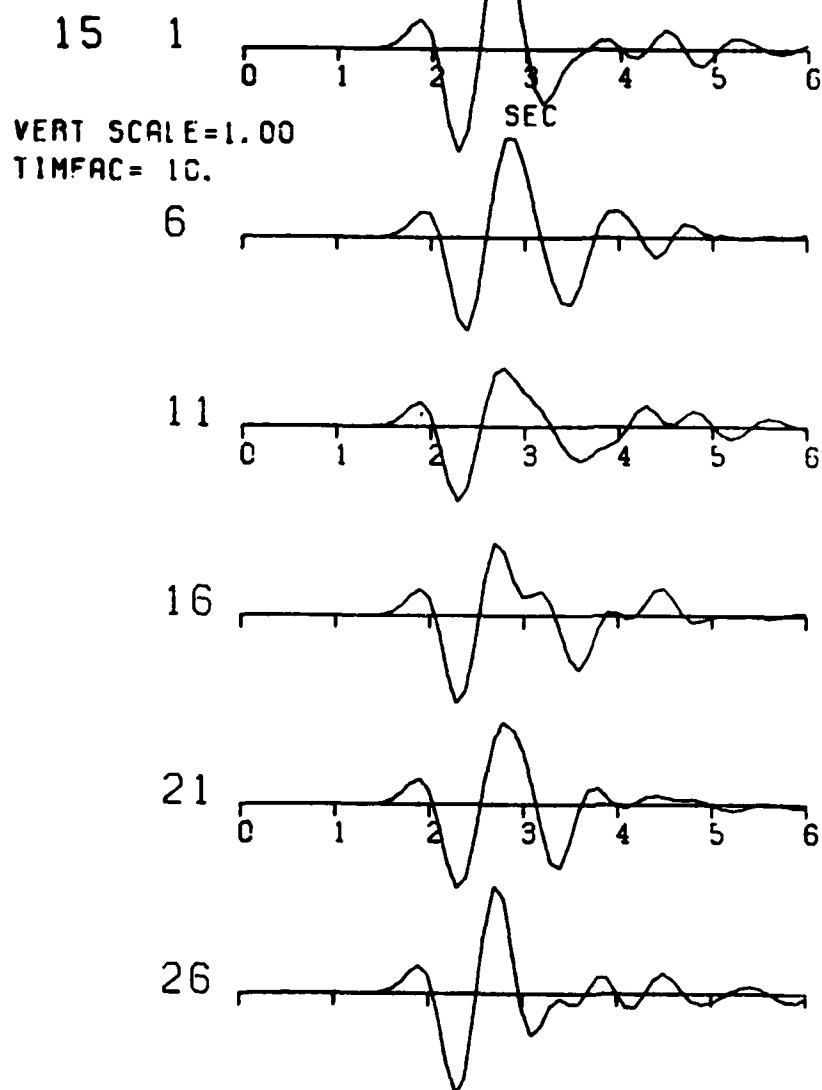


Figure 11. Ricker wavelet synthetic seismograms for North azimuth.

NTS BASIN-NORTH AZIMUTH EXPLOSION SOURCE

ROW COL

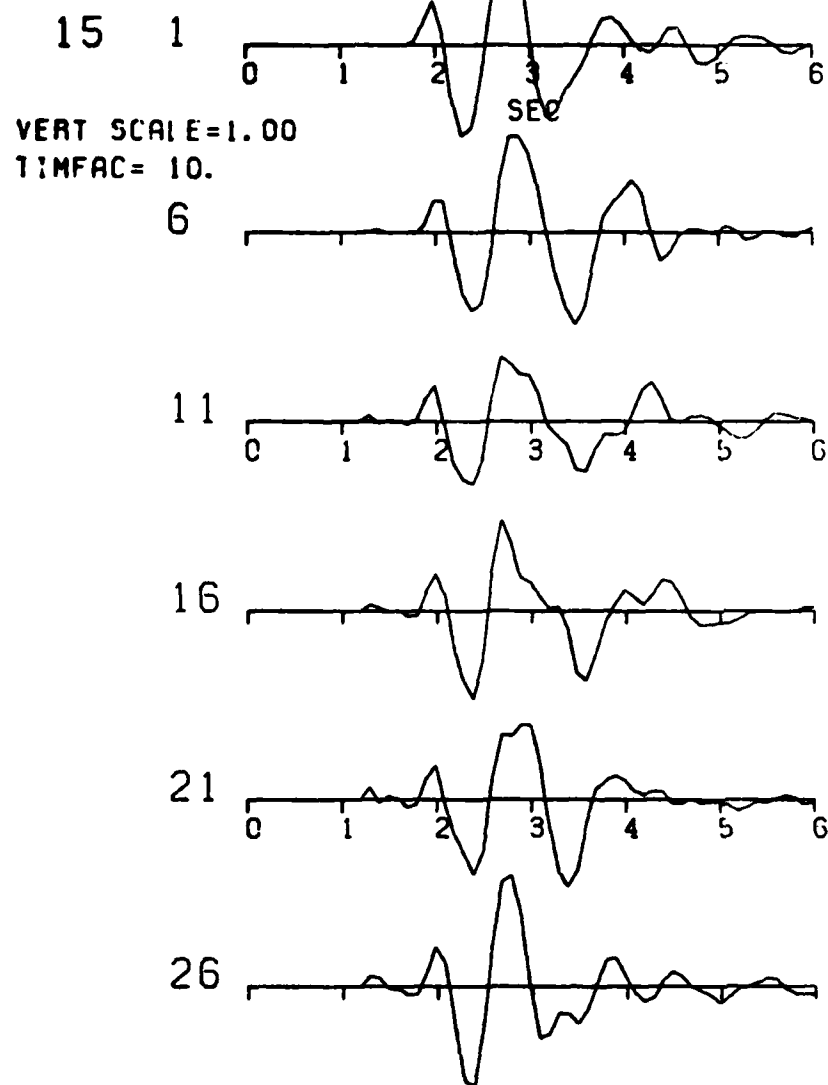
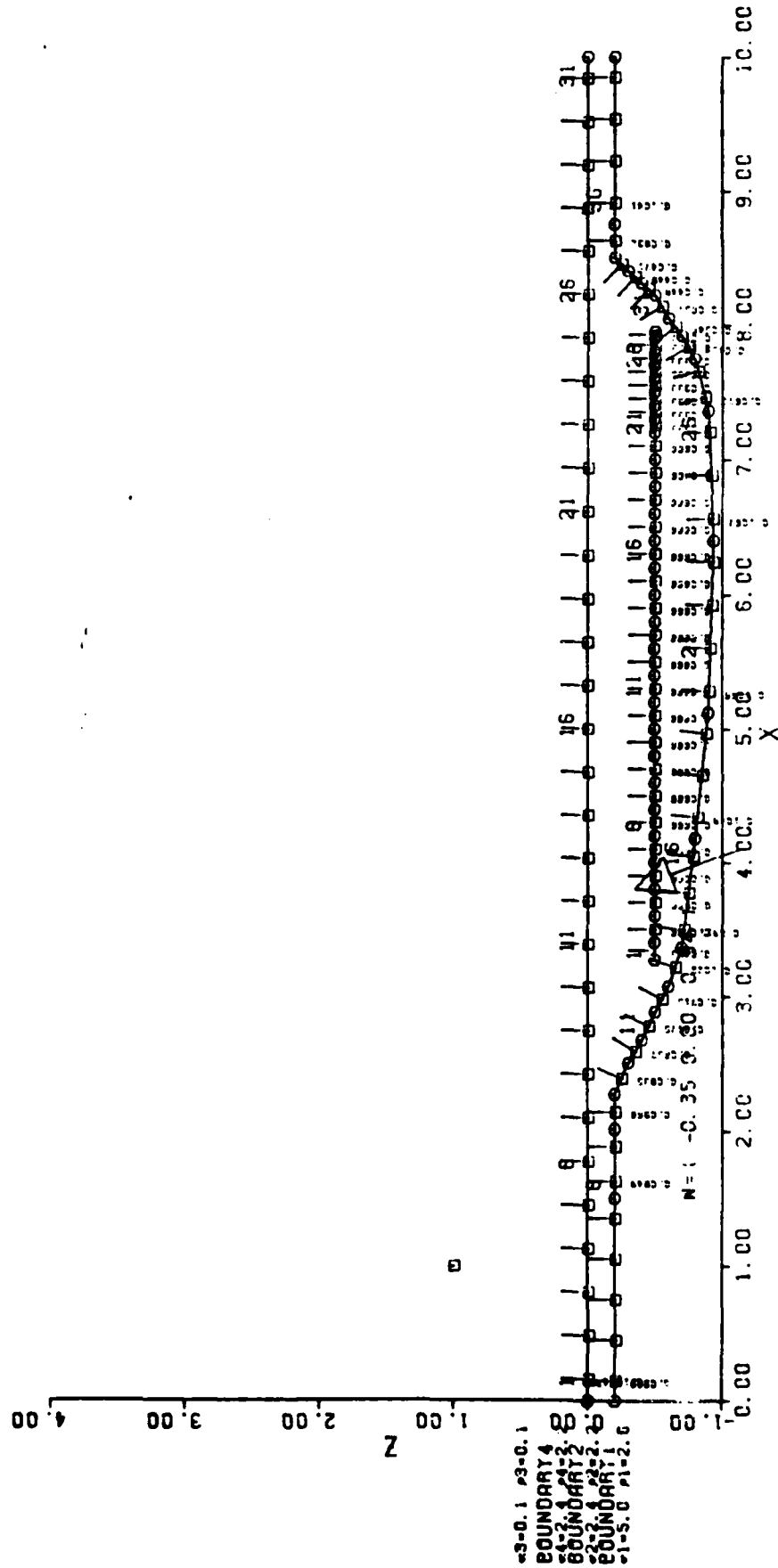


Figure 12. Synthetic seismograms, as in Figure 8 but for North azimuth.

NTS BASIN EAST AZIMUTH

MAX SPACE=0.3330



BOUNDARY 1
INIT DATA 22 PTS.
SPACED GRID 39 PTS.

BOUNDARY 2
INIT DATA 2 PTS.
SPACED GRID 31 PTS.

BOUNDARY 3
INIT DATA 29 PTS.
SPACED GRID 28 PTS.

Figure 13. Model as in Figure 5, but for East azimuth.

NTS BASIN
EAST AZIMUTH

30

ROW COL

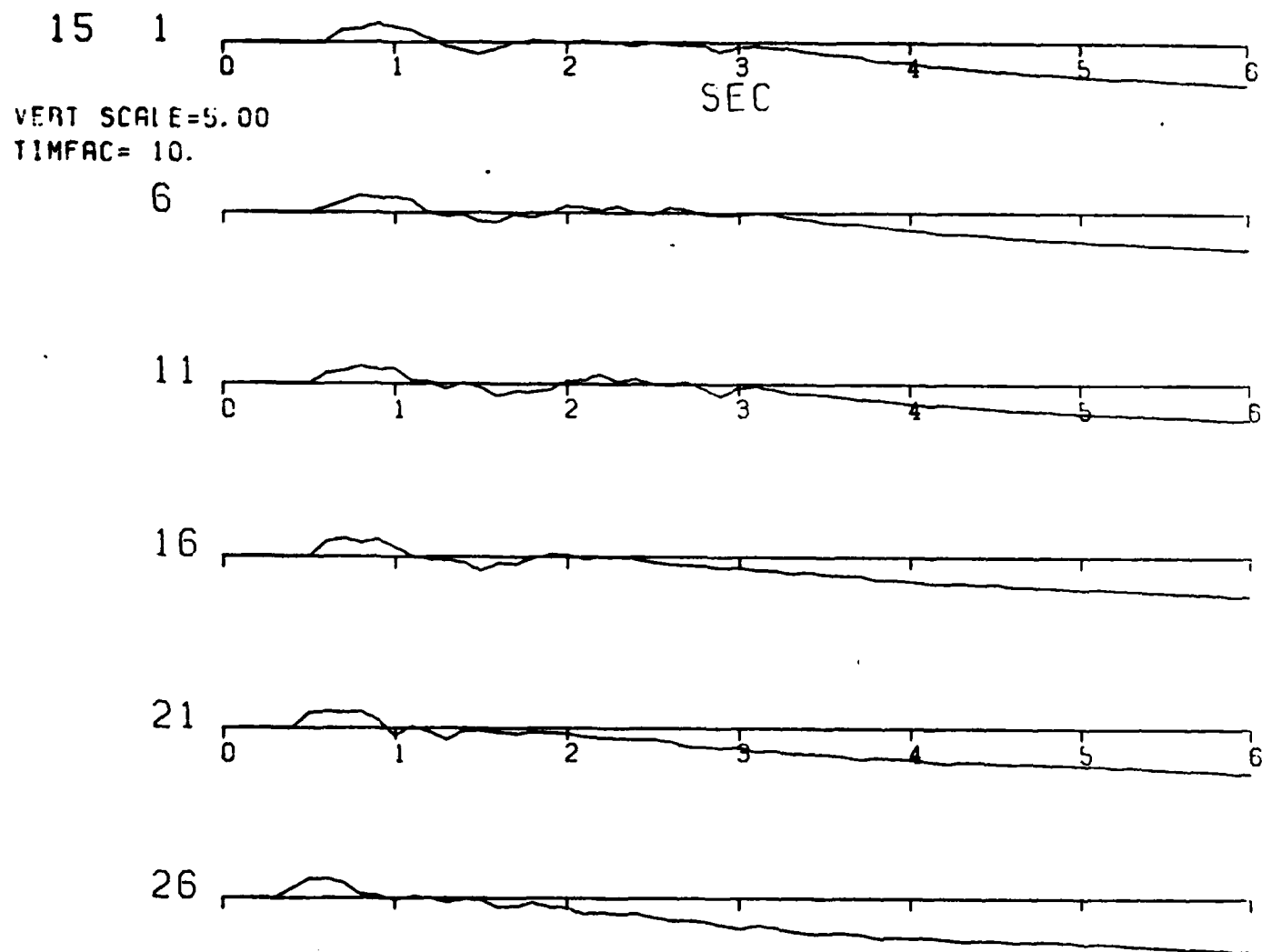
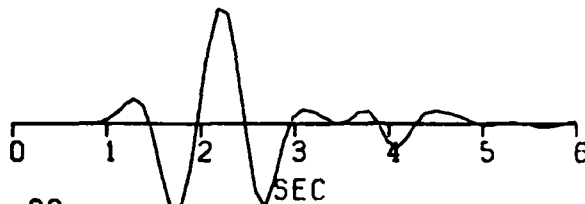


Figure 14. Step function responses for East azimuth.

NTS BASIN-EAST AZIMUTH
WAVELET SOURCE

ROW COL

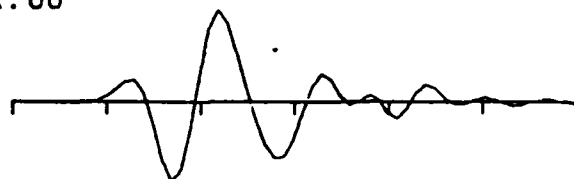
15 1



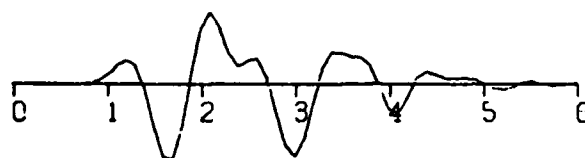
VERT SCALE=1.00

TIMFAC= 10.

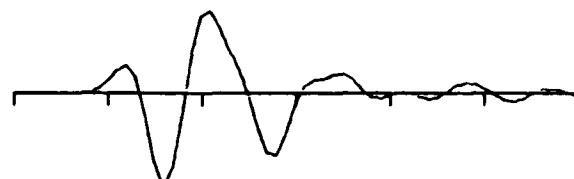
6



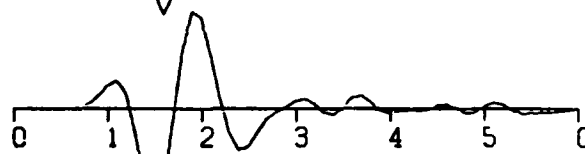
11



16



21



26

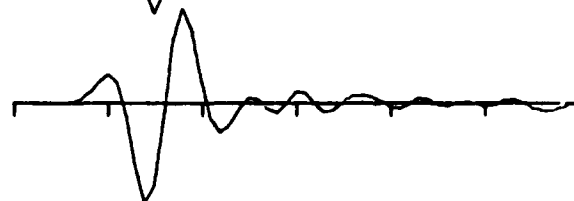
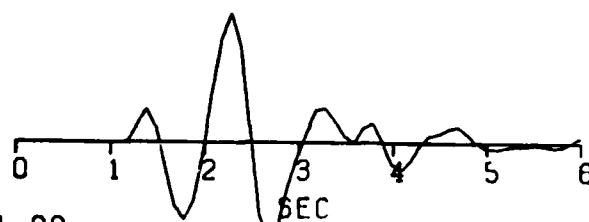


Figure 15. Ricker wavelet synthetic seismograms for East azimuth.

NTS BASIN-EAST AZIMUTH EXPLOSION SOURCE

ROW COL

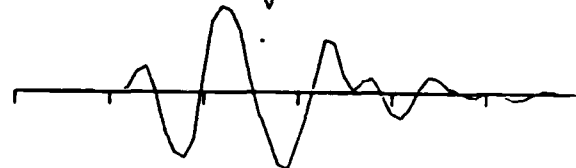
15 1



VERT SCALE=1.00

TIMFAC= 10.

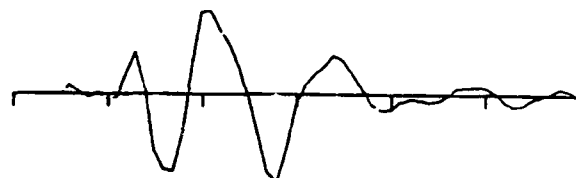
6



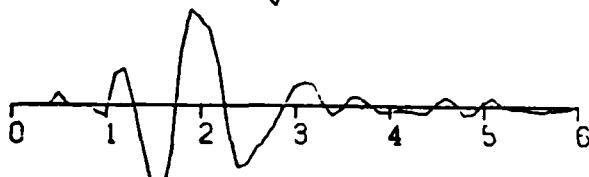
11



16



21



26

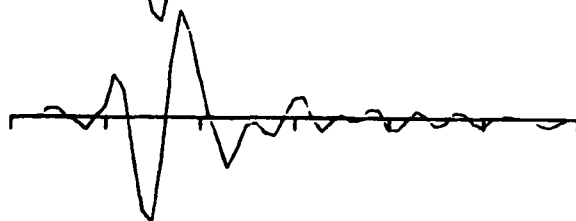


Figure 16. Synthetic seismograms, as in Figure 8 but for East azimuth.

amplitude. As the multiple reflections move still further back in time, for sources 11 and 16, we lose the constructive interference effect, with a resultant decrease in amplitude and the development of an inflection in the second peak. Near the eastern portion of the basin, (sources 21 and 26), we find an increase in amplitude and decrease in pulse width, due to the proximity of the eastern wall.

A comparison of Figures 7 and 8 shows that while details of waveforms differ, the overall trends in amplitude and waveform are the same for the Ricker wavelet and explosion source synthetics. This fact indicates that even though these effects are caused by interference of several arrivals, they are not unduly sensitive to small changes in source function.

The model and synthetic seismograms appropriate to a northern azimuth are presented in Figures 9-12. While the northern azimuth results differ in detail from those for the eastern azimuth (Figures 13-16), the overall trends are the same, in terms of both amplitude and waveform. In general, somewhat less overall amplitude variation is present for both of these azimuths in comparison to the amplitude variation occurring for a western azimuth. It is also somewhat surprising that synthetics for source 26 show smaller amplitudes, at all azimuths, than synthetics from other source locations. This appears to be related to the large slope of the basin to the east. It is not known at this time, however, whether this effect is real or merely an artifact of the Kirchhoff approximation.

The predicted amplitude anomaly as a function of source location and azimuth is summarized in Table 2. No attempt has been made here to correct for either period or instrument. In terms of general trend, the decrease in apparent magnitude from the western edge to the center

SGI-R-82-058

TABLE 2

NTS Predicted Magnitude Anomalies

		AZIMUTH		
		W	N	E
Source	1	.30	.18	.15
Location	6	.11	.11	.08
	11	.10	-.02	.00
	16	.00	.02	.08
	21	.04	.06	.13
	26	.08	.15	.13

of the basin agrees well with the results of Alewine et al. (1977) shown in Figure 1. Comparison with a more recent study by Alewine (personal communication), shown in Figure 17, do not, however, show good agreement in detail. For reference, Figure 18, which shows line A-A', is scaled identically with Figure 17. It cannot be presently determined whether the discrepancy is due to lack of a sufficiently accurate or detailed basin model, to inadequacies in m_b as a measure of event size when interference effects produce large changes in apparent period, or to some other factor.

The predicted evolution of waveforms as a function of location in the basin provides a test of the validity of the modeling procedure. Figure 18 shows the basement structure, the line A-A and the location of nine underground nuclear explosions in reasonably close proximity to line A-A'. Available seismograms for these events at ZOBO, MAJO and NAO are shown in Figures 19-21. A projection of these events onto line A-A' was done in such a way as to preserve the distance from the eastern edge of the basin. The time scale of the observed seismograms in the figures is the same scale used in the synthetics.

Due to the symmetry of the basin, seismograms recorded at ZOBO (a southerly azimuth), Figure 19, should be comparable to synthetics for a northern azimuth. The evolution of the inflection in the second peak and development of the second trough as predicted by the synthetics when the source is moved toward the center of the basin can clearly be seen in the data. The trend in the synthetic waveforms is thus confirmed, despite the fact that no attempt was made to correct source time functions or depths for individual events.

YUCCA VALLEY MAGNITUDE RESIDUALS (OBSERVED - PREDICTED)

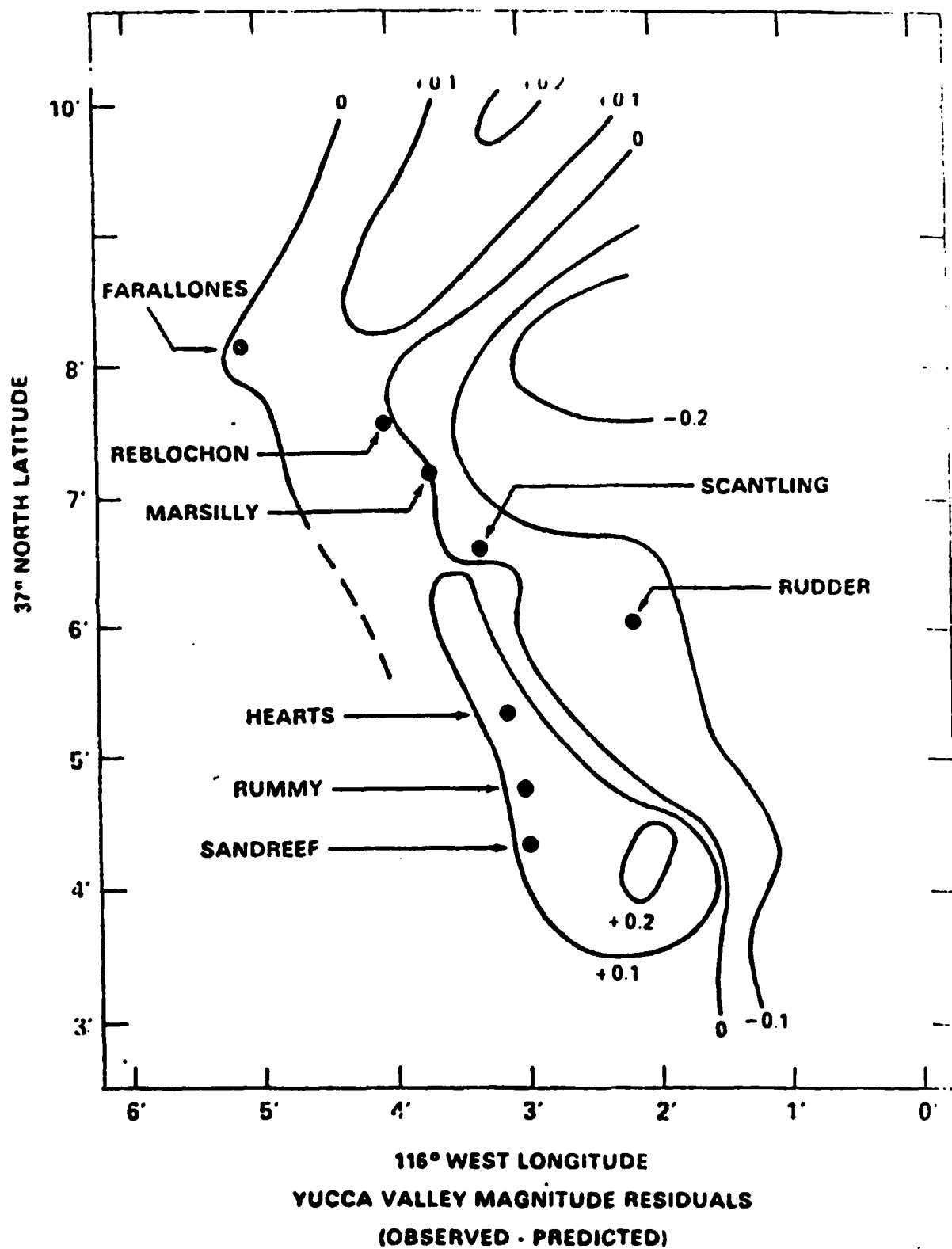


Figure 17. (after Alewine, et al. 1977) Observed magnitude residuals for Yucca Flats.

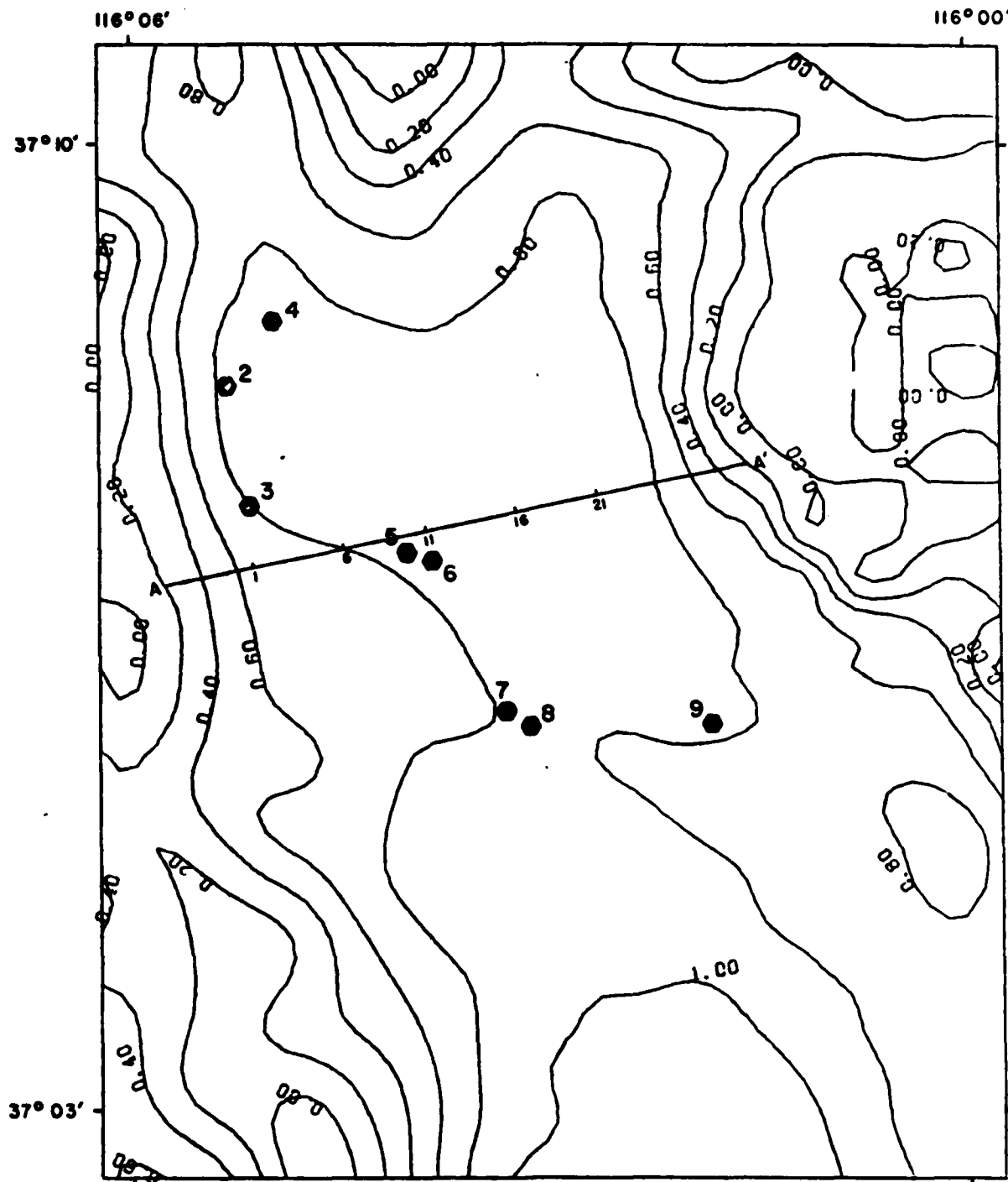


Figure 18. Expanded version of Figure 2 showing depth to Cenozoic-Paleozoic contact, in km. Line A-A' corresponds to cross sections in Figures 5, 9, and 13, with source locations indicated. Hexagonal symbols indicate locations of events used for waveform comparisons.

The seismograms for MAJO, shown in Figure 20, show a great similarity to the ZOBO seismograms. The moveout of the Cenozoic-Paleozoic interface reflection is even more obvious for this station than for ZOBO. Once again, good qualitative agreement is obtained between synthetic and observed waveforms, although it appears that the synthetics have somewhat underestimated the size of the reflected arrival.

Seismograms recorded at NAO once again exhibit approximately the same predominant period as do the synthetics. As with the other data, we see a general trend toward broadening and development of an inflection as we move the source toward the center of the basin. For this station, however, it is more apparent than for the previous two stations, that detailed agreement between data and synthetics is lacking although general trends do appear to be correct.

We now consider sources in the southern portion of the basin. A two-dimensional model, based on the Herrin E-3 profile (shown in Figure 3 with material properties shown in Table 1) was used in this phase of the study. It was also necessary to modify this model to insure numerical stability of the Kirchhoff integral code. This was done by tapering both ends of the basin in order that no layer thickness is reduced below 200 m. We have elected, in this case, to retain the water table in the model. The intermediate interface plays the dual role of source location and boundary between saturated and unsaturated tuff. Sources are located just below the water table.

ZOBO

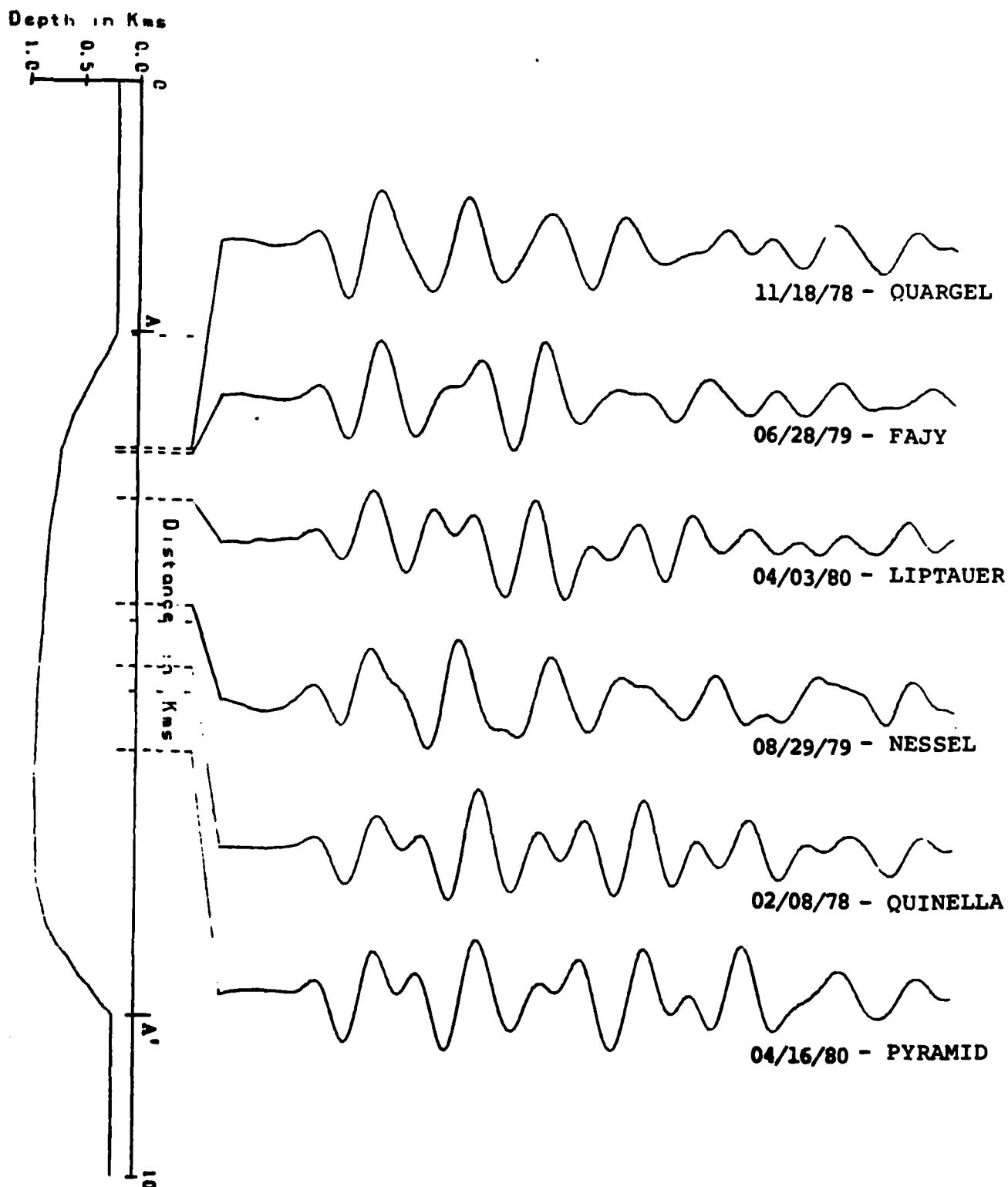


Figure 19. Waveforms of events proceeding east to west across basin, recorded at station ZOBO. Note development of interference effect on back of second peak. Traces scaled to equal amplitude by plotting routine.

MAJO

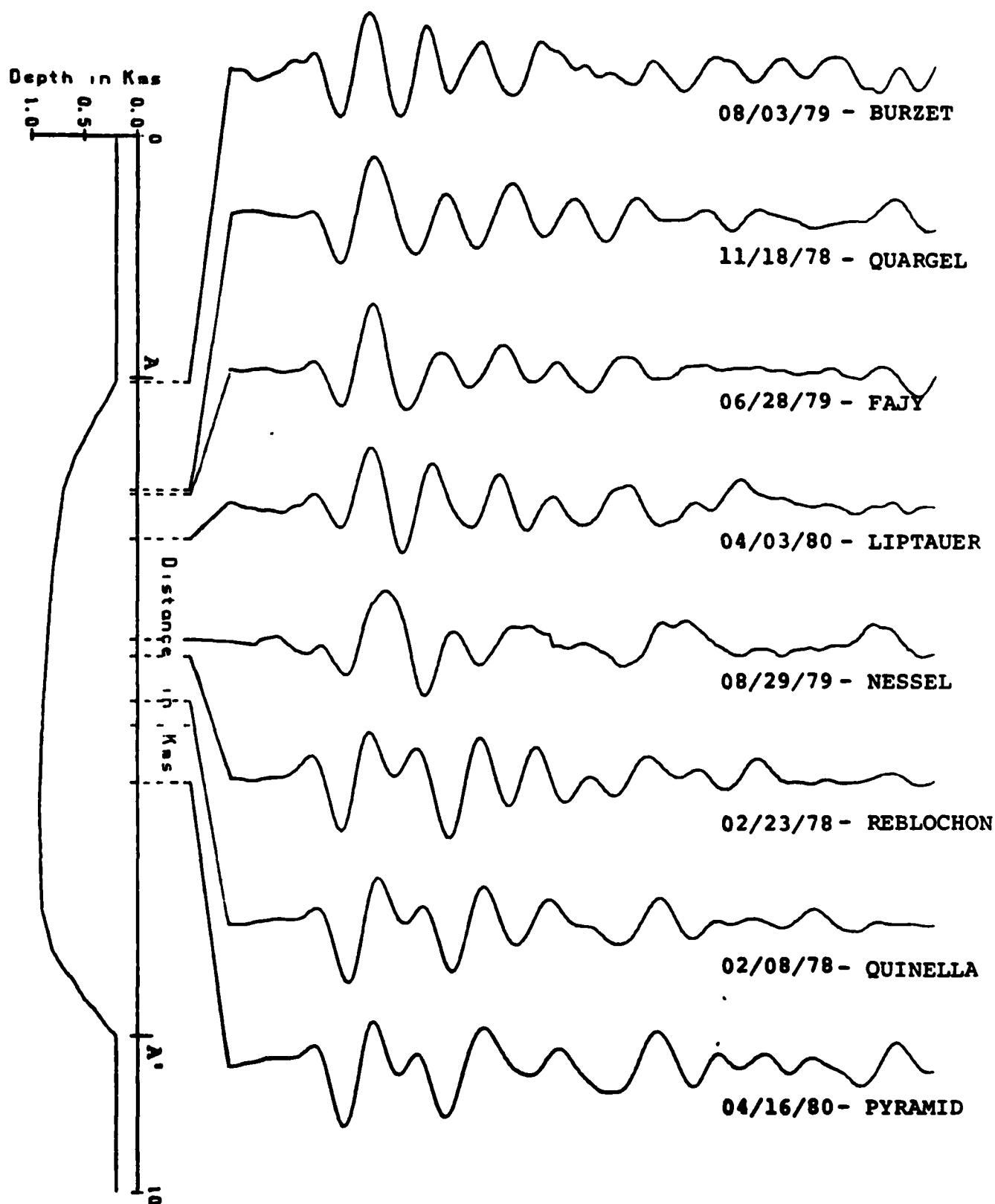


Figure 20. Waveforms recorded at station MAJO for events proceeding west to east across the basin.

NAO

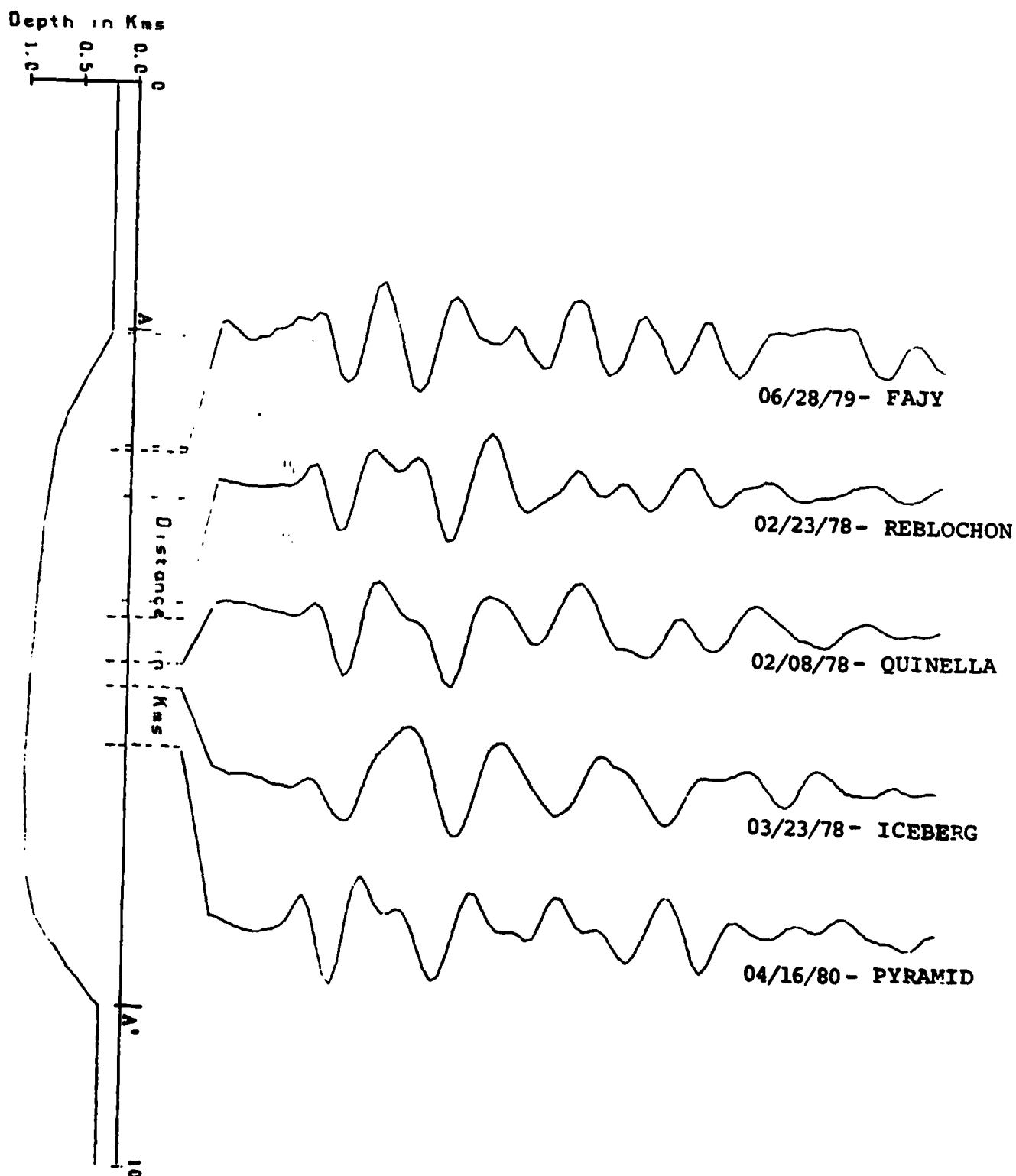


Figure 21. Waveforms recorded at station NAO for events proceeding west to east across basin.

Models and results for the northern azimuth are presented in Figures 22-25 and for the eastern azimuth in Figures 26-29. The synthetic seismograms in Figures 24, 25, 28 and 29 show a large amplitude increase for both azimuths for source location 7, located very near the boundary fault. Moving the source further east produces a relatively slight amplitude decrease with minimum amplitude occurring at source location 16, followed by an amplitude increase as the source is moved still further east. Some waveform variation is observed in the eastern part of the basin but, with the exception of source location 7, very little waveform change is evident in the western portion. Comparison of the amplitude behavior of the synthetics with the observed magnitude residuals in Figures 1 and 3 show some qualitative agreement.

Both the amplitude and waveform variation of the northern basin model contrast sharply with that observed for the southern basin model. The differences appear to be related to the extreme dip of the basement near the west side of the basin in the southern model. Numerical experiments have shown that the dip of this boundary fault controls the amplitude of the basement reflection which, in turn, creates the major portion of the amplitude and waveform variation observed for the northern model. As the dip of this feature increases, the amplitude of the reflection goes through a maximum for source locations east of the fault.

Since the Kirchhoff approximation does not correctly handle critical reflections and most diffractive effects, both of which will be present when extreme dips in structure occur, these observed effects could conceivably be an artifact of the modeling technique. Further study would be required to answer this question.

NTS PROFILE E-3 ON-Axis

MAX SPACE=0.3300

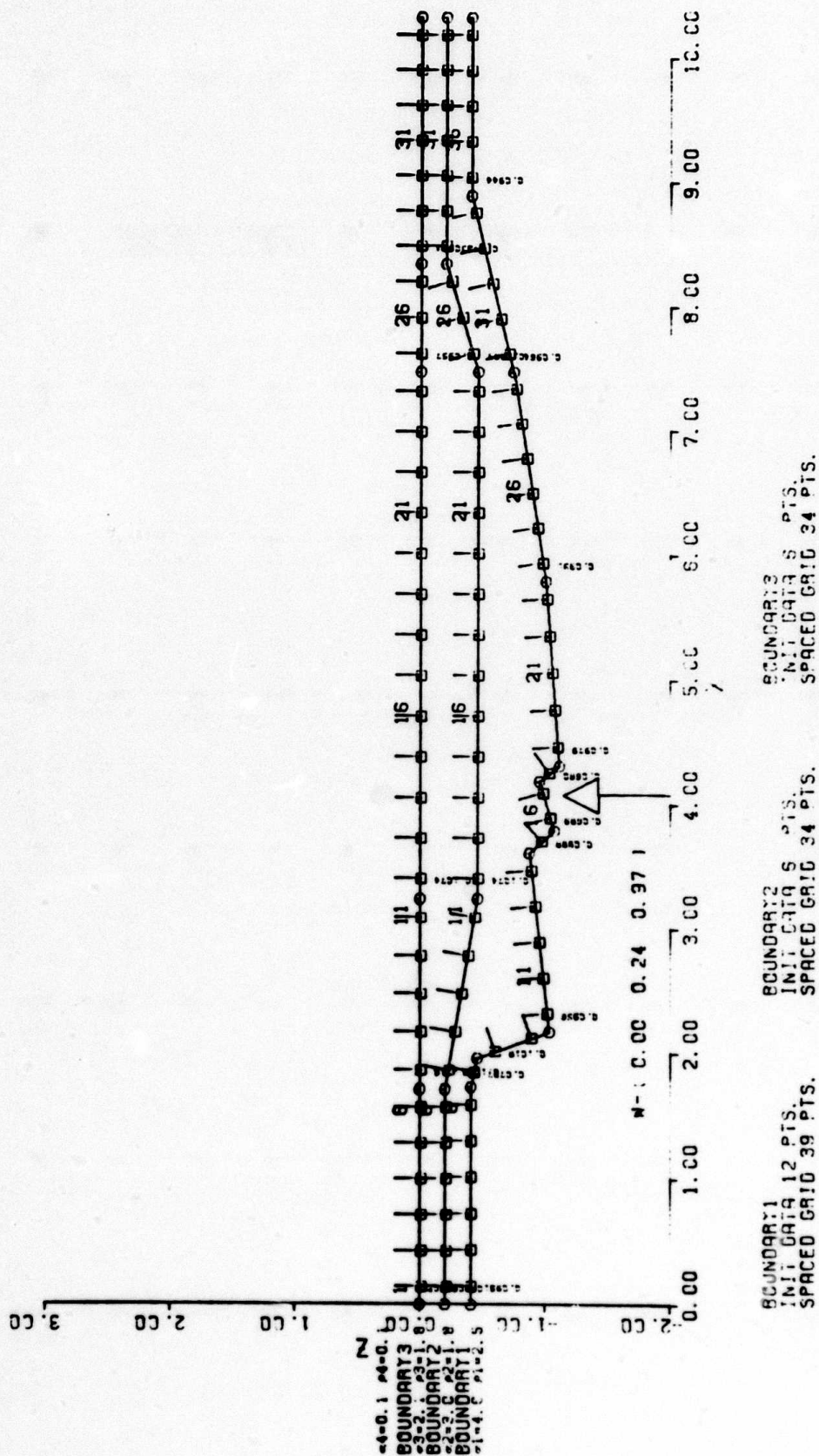


Figure 22. Herrin et al. profile E-3, used as cross section for two-dimensional southern basin model. Grid shown for surface, water table and Paleozoic interface. Sources located directly below water table. For receiver at northern or southern azimuth.

NTS PROFILE E-3 ON-AXIS

ROW COL

15 7

VERT SCALE=5.00
TIME=10.

10

13

16

19

22

25

0 1 2 3 4 5 6
SFC

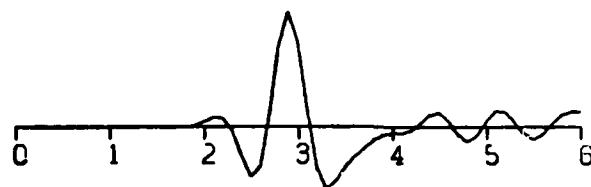
Figure 23. Step function responses for model in Figure 23 at north or south azimuth.

ON-AXIS

WAVELET SOURCE

ROW COL

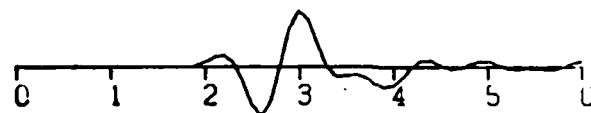
7



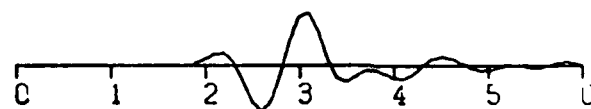
VERT SCALE=2.00

TIMFAC= 10.

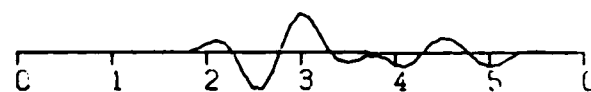
10



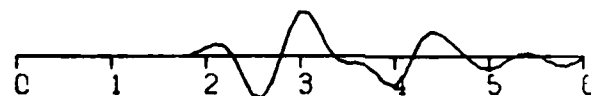
13



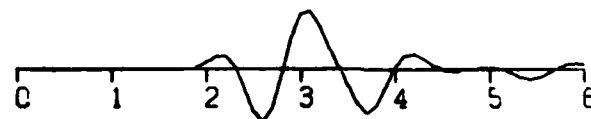
16



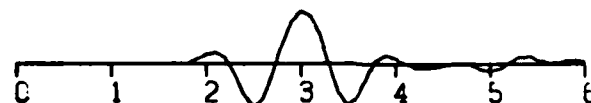
19



22



25



28

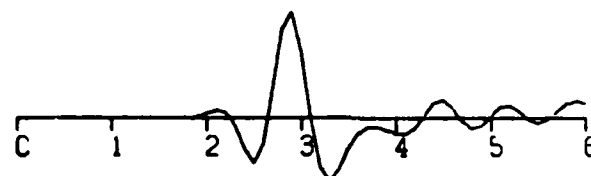


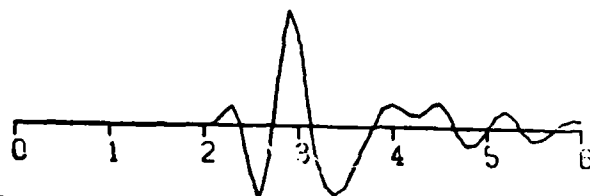
Figure 24. Ricker wavelet source synthetics for model in Figure 22 and receiver at north or south azimuth.

ON-AXIS

EXPLOSION SOURCE

ROW COL

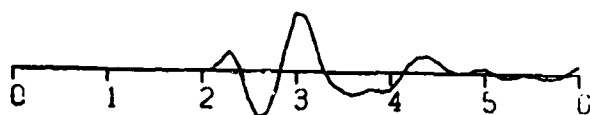
7



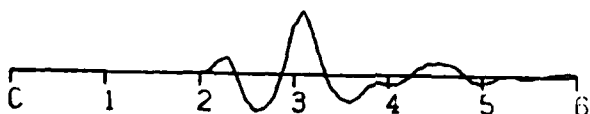
VERT SCALE=2.00

TIMFAC= 10.

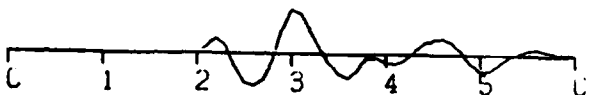
10



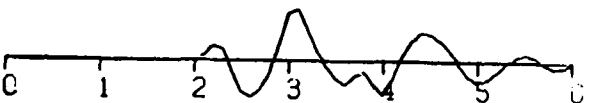
13



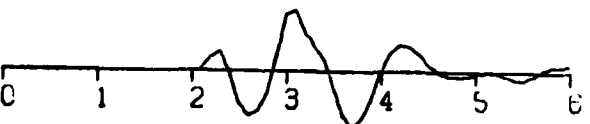
16



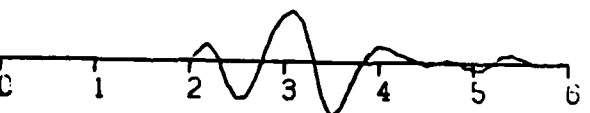
19



22



25



28

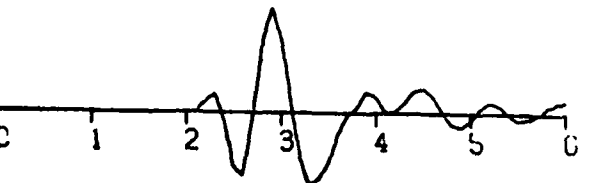


Figure 25. Synthetic seismograms for explosion sources, as in Figure 8, but for model in Figure 22 with receiver at north or south azimuth.

NTS PROFILE E-3 OFF-AXIS EAST

MAX SPACE=0.3300

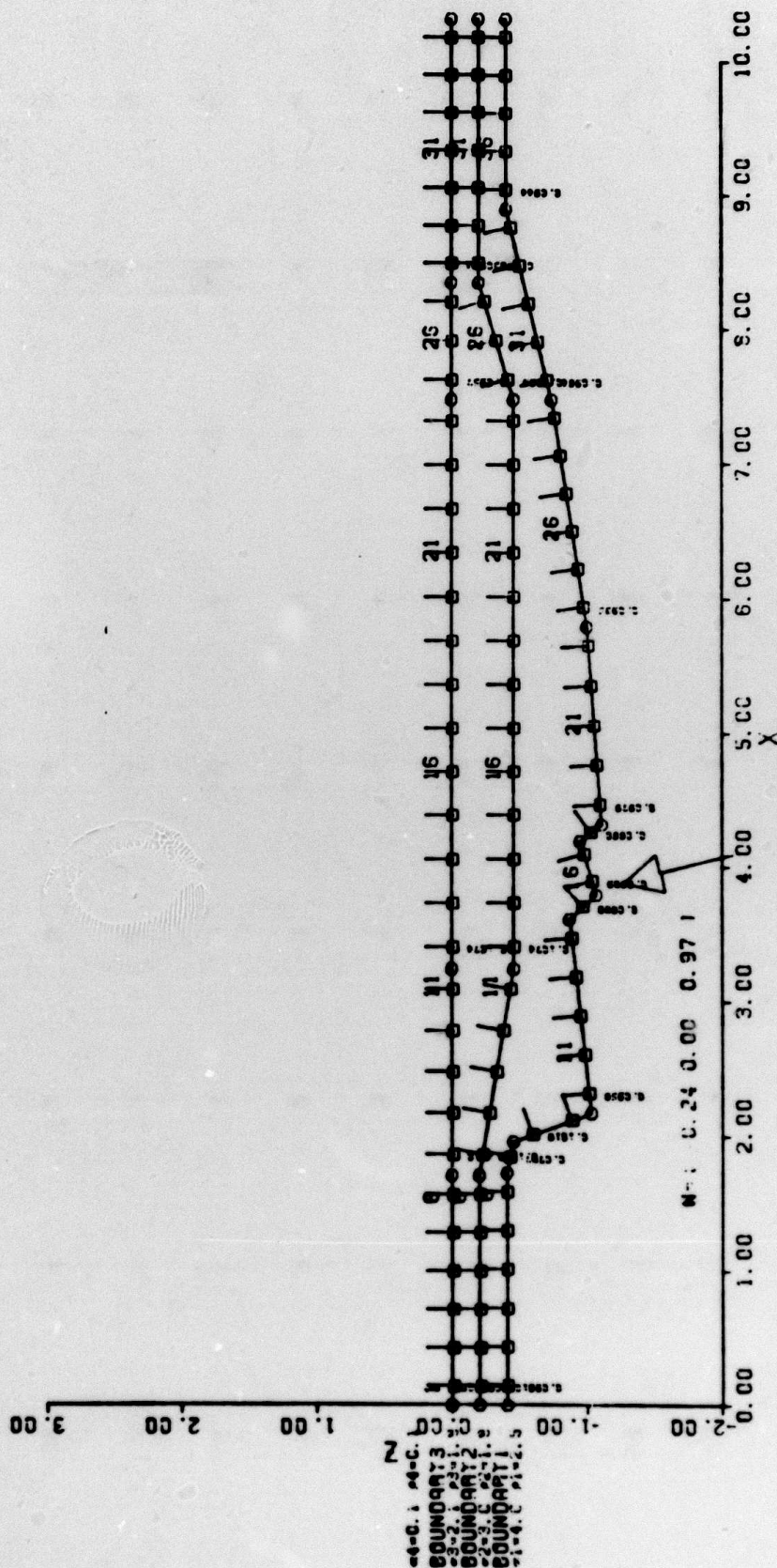


Figure 26. Model as in Figure 22 but for receiver at east azimuth.

NTS PROFILE E-3
OFF-AXIS EAST

ROW COL

15 7

VERT SCALE=5.00
TIMEFAC= 10.

10

13

16

19

22

25

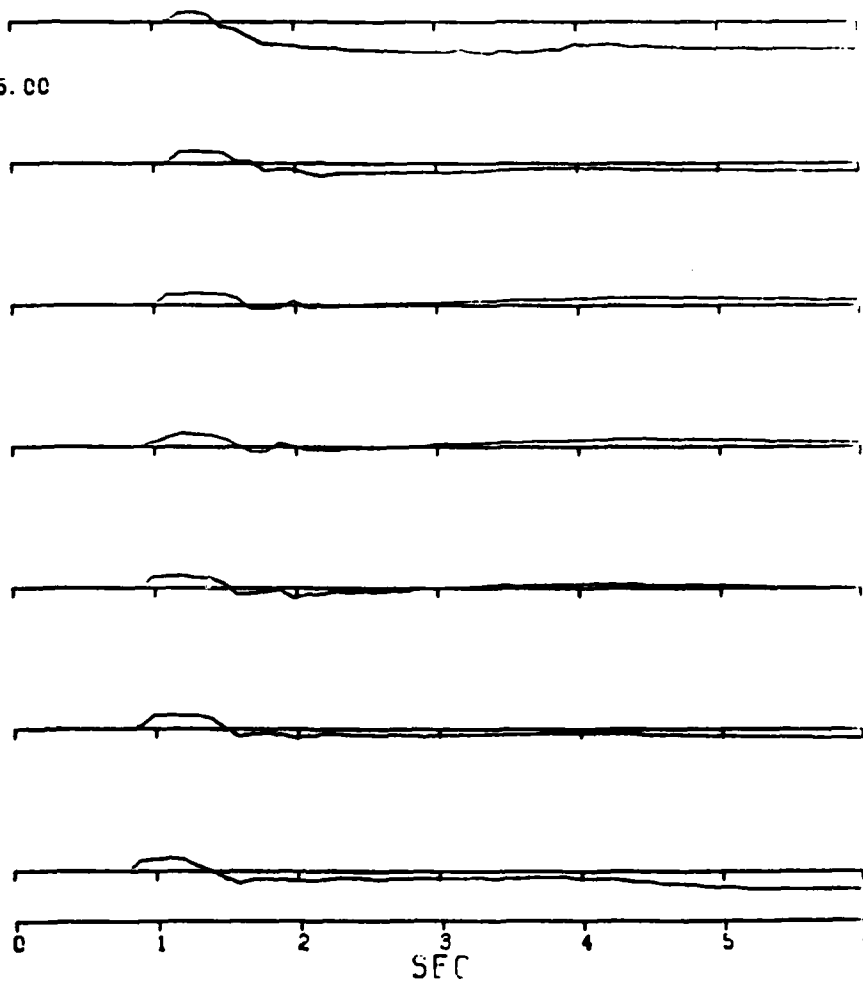


Figure 27. Step function responses for sources in Figure 26.
Receiver at east azimuth.

NTS PROFILE E-3
OFF-AXIS EAST
WAVELET SOURCE

ROW COL

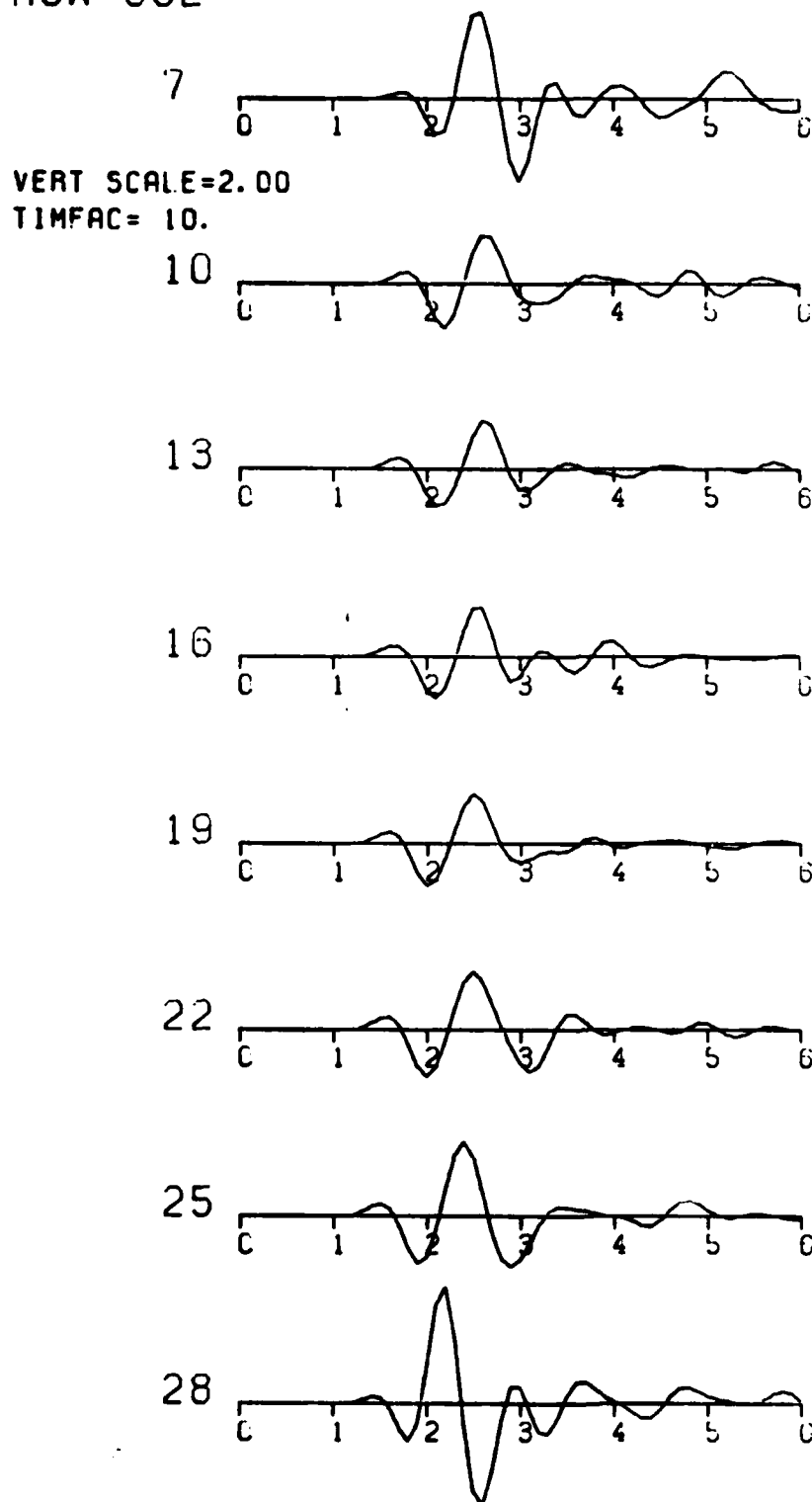


Figure 28. Ricker wavelet synthetic seismograms for model in Figure 26. Receiver is at east azimuth with $p = .07 \text{ sec/km}$.

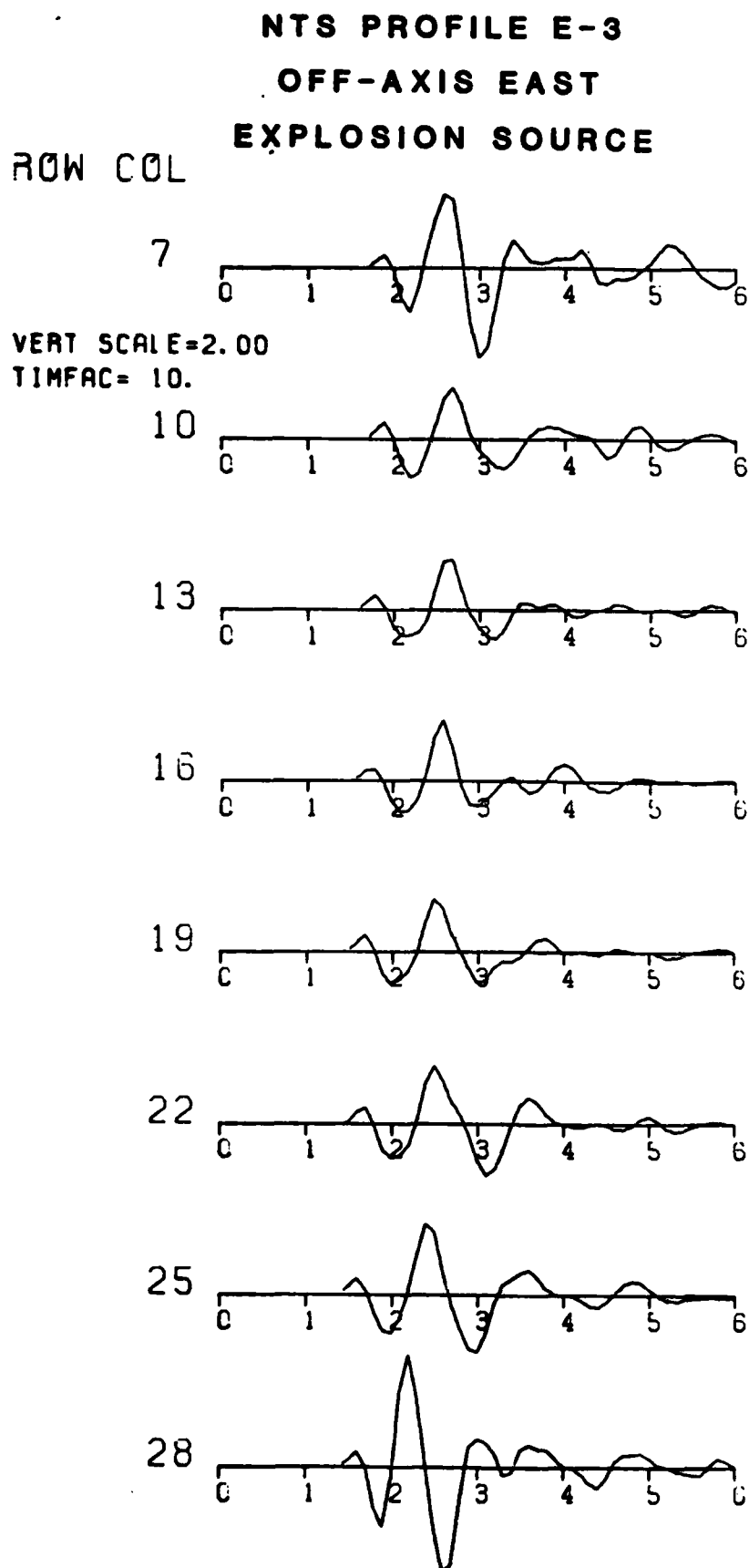


Figure 29. Synthetic seismograms as in Figure 8 but with model in Figure 26. Receiver is at east azimuth.

4. Conclusions and Recommendations

The Kirchhoff integral approximation has proved to be a useful tool in examining the effects of shallow structure on body wave amplitudes and waveforms from underground nuclear explosions. In the example of Yucca Flats, it has been possible to broadly model the observed waveform variation and essentially all of the observed amplitude variations in the northern portion of the basin solely by modeling interactions with the Paleozoic-Cenozoic contact. Differences in the finer details do, however, exist between the observations and predictions. Several important conclusions and observations can be drawn from this modeling effort. Among the more significant is the fact that the waveform and amplitude variations are the result of interference effects resulting from known shallow structure and are not the result of focusing caused by deep structures. In addition, it is clear that these interference effects are controlled by the impedance contrast at the Paleozoic-Cenozoic contact and, particularly with respect to the extent and spatial location of the interference, by the steeply dipping sidewalls of the basin. These facts suggest that an accurate knowledge of depth of burial and source time function is essential to matching the finer details of the seismic radiation from this region.

Although one can confidently state that the amplitude and waveform variations at Yucca Flats have been satisfactorily modeled, there are other lines of related research that should be considered for further study. The first of these involves the use of more sophisticated global approximation boundary integral equation techniques to deal with problems created by pinch-out of layers and by steeply dipping structures. These are apparent, for example, near the

boundary fault in the southern portions of Yucca Flats. This research is not required to confirm our conclusions with regard to the Yucca Flats anomalies but would provide valuable parameters and understanding for analysis of future source locations of interest.

III. RECEIVER FUNCTIONS APPROPRIATE TO NTS

The purpose of this study is to estimate relative receiver functions for the Nevada Test Site Global Array (NTSGA) which is composed of all high quality digital seismic stations in the distance range 30° to 90° from the source location. Relative receiver functions (RRF's) model all near-receiver contributions to observed waveforms at stations in the array relative to the reference station. The computed receiver functions will permit more complete forward modeling of synthetic seismograms of NTS nuclear explosions as observed at stations within the array.

The calculation of relative receiver functions is done in two steps. First, trace deconvolutions are computed by spectral ratio of the trace at a secondary station to the trace at a reference station. The trace deconvolutions are computed for each event in the data set for which both reference and secondary station seismograms are available, and the results for each station pair are averaged in the log-frequency domain. The result is an average transfer function which permits computation of a synthetic trace from the reference seismogram.

The second step involves the recovery of the receiver functions from the deconvolutions with the additional constraint that the receiver functions are as simple or "delta-like" as is consistent with the information in the trace deconvolutions. This can be done by finding a linear operator which, when convolved with trace deconvolutions, will maximize the order (or minimize the entropy) in the set of estimated receiver functions as a whole. Although the entropy minimum found is not unnecessarily unique, tests have shown that the significant information in a set of receiver functions determined by well-constrained trace

deconvolutions is stable as a function of reference station, number of secondary stations, and choice of weighting schemes.

There are 16 stations which qualify for the NTSGA, including SRO, LRSM, and NORSAR stations. The SRO station ZOBO in Bolivia was chosen as the reference station because it had more useful traces than any of the other stations in the array, and because tests showed that ZOBO seismograms have high frequency character relative to the rest of the array.

Selecting ZOBO as the reference station allowed the use of 17 NTS events between May 1977 and September 1980. Eleven of the 15 secondary stations in the NTSGA had four or more usable trace pairs with ZOBO for these events. Although we have obtained all useful data from the SRO stations for this time period, gaps in data exist for the AEDS stations from May 1977 to December 1977 and September 1978 to June 1979.

Estimated relative receiver functions were computed for the twelve stations using MED processing. Based on the complexity and frequency content of the computed receiver functions, it appears that ZOBO was not the best choice for a reference station. However, KONO, which might have been considered as a better reference station, failed to provide enough data to be used as the reference station.

The use of receiver functions as deconvolution filters is briefly examined. The problems include bandwidth and noise, but the most important concept developed is that receiver functions are designed as convolution filters and thus are not appropriately used in a deconvolution sense. Further research will be required to define filters which may be used to simplify observed seismograms prior to magnitude estimation.

A detailed presentation of the results of this study is given by Lundquist et al. (1981) (VSC-TR-81-026).

IV. MOTIVE FUNCTIONAL SPECIFICATIONS

A number of techniques are currently available for seismic discrimination and yield estimation. Most of these methods, however, fail to fully utilize the available azimuthal information and, indeed, many methods for magnitude estimates use only a single amplitude measure. Shallow earthquakes will, in general, produce waveforms and amplitude patterns that vary azimuthally while a pure explosion in theory produces azimuthally independent waveforms and amplitudes. This fact is not utilized in most discrimination schemes. In the yield estimation context, azimuthal variations in waveform and amplitude may contain information on tectonic release for which a correction should be, but is usually not, made in obtaining yield estimates. In the technical report on the subject (VSC-TR-21-22), we describe a computer program, MOTIVE, which makes use of this azimuthal information, as well as utilizing significant portions of the waveform information, in both discrimination and yield estimation contexts.

MOTIVE is a joint body wave and surface wave moment tensor inversion program. Given properly windowed body wave and surface wave seismograms and a trial depth, MOTIVE determines the second order moment tensor that provides the best fit, in a least squares sense, of synthetics to the data. By using a number of trial depths and selecting the depth that produces the minimum error, depth, as well as source type and orientation, may be determined.

MOTIVE incorporates several unique features in addition to the joint use of body wave and surface wave data. The user can specify any of four source types; an unconstrained moment tensor, an isotropic source, a double couple source and a double couple plus isotropic

source. This gives the user the ability to explore the sensitivity of his solution to the most commonly made physical assumptions about the source. Moreover, MOTIVE can include state-of-the-art body wave and surface wave path and receiver corrections, determined for each source-station pair. This should help eliminate one of the major sources of error and bias in moment tensor estimation, particularly where short-period body wave seismograms are used.

A flexible modular approach has been used in developing MOTIVE, in order that the same program, through choice of user options, may be used for both routine processing and research. This flexibility also insures that future improvements can be readily incorporated into the existing program structure.

Seismograms recorded at NAO once again exhibit approximately the same predominant period as do the synthetics. As with the other data, we see a general trend toward broadening and development of an inflection as we move the source toward the center of the basin. For this station, however, it is more apparent than for the previous two stations, that detailed agreement between data and synthetics is lacking although general trends do appear to be correct.

We now consider sources in the southern portion of the basin. A two-dimensional model, based on the Herrin E-3 profile (shown in Figure 3 with material properties shown in Table 1) was used in this phase of the study. It was also necessary to modify this model to insure numerical stability of the Kirchhoff integral code. This was done by tapering both ends of the basin in order that no layer thickness is reduced below 200 m. We have elected, in this case, to retain the water table in the model. The intermediate interface plays the dual role of source location and boundary between saturated and unsaturated tuff. Sources are located just below the water table.

V. REFERENCES

- Alewine, R.W., Young, G.B., Springer, D.L. and Klepinger, R.W., (1977). Teleseismic P-wave magnitude-yield relations for well-coupled N.T.S. explosions. AFTAC-TR-77-22 (SECRET).
- Futterman, W.I. (1962). Dispersive body waves. J. Geophys. Res., 67, 5279-5291.
- Hart, R.S., Hadley, D.M., Mellman, G.R. and Butler, R. (1979). Seismic Amplitude and Waveform Research, Sierra Geophysics, Inc., Report SGI-R-79-012.
- Herrin, G., Goforth, T. and Ferguson, J. (1981). Semi-Annual Technical Report to the Air Force Office of Scientific Research.
- Von Seggern, D., and Blandford, R. (1972). Source time functions and spectra for underground nuclear explosions. Geophys. J. R. Astr. Soc., 31, 83-98.
- Wyss, K. and Mellman, G.R. (1982). Some approximate boundary integral equation methods for wave propagation in laterally heterogeneous media. In preparation.